

May 1986

NASA-TP-2553 19860016452

Description of Data on the Nimbus 7 LIMS Map Archive Tape

*Temperature and
Geopotential Height*

Kenneth V. Haggard,
Ellis E. Remsberg,
William L. Grose,
James M. Russell III,
B. T. Marshall,
and G. Lingenfelser

LIBRARY COPY

MAY 2 1986
LANGLEY RESEARCH CENTER
LIBRARY, NASA
HAMPTON, VIRGINIA

1986

Description of Data on the Nimbus 7 LIMS Map Archive Tape

*Temperature and
Geopotential Height*

Kenneth V. Haggard,
Ellis E. Remsberg,
William L. Grose,
and James M. Russell III

*Langley Research Center
Hampton, Virginia*

B. T. Marshall
*SASC Technologies, Inc.
Hampton, Virginia*

G. Lingenfelser
*Analytical Mechanics Assoc., Inc.
Hampton, Virginia*



National Aeronautics
and Space Administration

Scientific and Technical
Information Branch

Introduction

The Limb Infrared Monitor of the Stratosphere (LIMS) experiment used a thermal infrared limb scanning radiometer with six channels centered at wavelengths ranging from $6.2\ \mu\text{m}$ to $15.0\ \mu\text{m}$ (see Russell and Gille 1978; Gille, Bailey, and Russell 1980; and Gille and Russell 1984). The experiment was turned on in orbit on October 24, 1978, and it operated nearly flawlessly for the planned $7\frac{1}{2}$ -month lifetime until May 28, 1979, measuring vertical radiance profiles across the atmospheric limb of the Earth. These profiles were later processed on the ground to infer middle atmosphere temperature profiles and the concentrations of key compounds believed to be important in stratospheric ozone photochemistry. The experiment lifetime was limited by the $\text{NH}_3\text{-CH}_4$ solid cryogen cooler used to cool the six HgCdTe detectors to a temperature of 64 K. The six channels included two in the $15\text{-}\mu\text{m}$ carbon dioxide (CO_2) band for two-color temperature-pressure sensing and others at $11.3\ \mu\text{m}$ for nitric acid (HNO_3) retrieval, $9.6\ \mu\text{m}$ for ozone (O_3), $6.9\ \mu\text{m}$ for water vapor (H_2O), and $6.2\ \mu\text{m}$ for nitrogen dioxide (NO_2). The standard approach for thermal infrared remote sensing was used. First, by measuring emission in the band of a gas whose mixing ratio is known (i.e., CO_2), the temperature profile was inferred; then by measuring emission in other bands, the unknown mixing ratios were retrieved. Since the observed parameter was horizon thermal emission, data were collected both night and day over the planned $7\frac{1}{2}$ -month experiment lifetime. The measurements were made nearly continuously during the mission with a duty cycle of 11 days on and 1 day off.

The LIMS radiometer scanned the atmospheric horizon (limb) vertically once every 12 seconds (84 km along the ground track) and obtained radiance profiles in each of six spectral bands as a function of tangent height. Tangent height is defined as the point of closest approach of a ray path to the Earth's surface (fig. 1). The instrument view direction was 33.5° counterclockwise from the negative spacecraft velocity vector so as to provide uniform coverage (fig. 2) in the Northern Hemisphere for the 99.3° orbital Sun-synchronous inclination. The geometry provided daily coverage from 64°S to 84°N . The upward and downward arrows in figure 2 denote ascending (generally daytime data) and descending (generally nighttime data) nodes for the approximately 14 orbits that occurred each day. The repeat cycle over a given latitude and longitude was about 6 days. The altitude coverage varied for each channel depending mostly on signal-to-noise ratio (S/N). The range for temperature and ozone was 10 km to

65 km, and for NO_2 , HNO_3 , and H_2O it was 10 km to 50 km. The lower altitude limit varied with latitude, being highest in the tropics because of interference by high clouds and lowest in the high latitudes. Also, at certain times, mostly during the high latitude deep winter period, the S/N became too low in the NO_2 and H_2O channels for certain regions where the temperatures were cold. This comment applies mostly to latitudes greater than about 60°N and for pressures greater than about 10 mbar. The instantaneous vertical field of view of the measurements was 1.8 km in the temperature, O_3 , and HNO_3 channels and about 3.6 km in the NO_2 and H_2O channels. Horizontal resolution was much more coarse and was dictated by the limb geometry and atmospheric absorption characteristics to be 18 by 300 km. The actual vertical resolution for the temperature data is about 2.5 km. This means that a 2-K amplitude feature of 5-km vertical wavelength can just be detected in these temperature data.

An extensive program of correlative balloon underflights was carried out to aid in validation of LIMS data. The intent of the program was to obtain comparative data under a variety of atmospheric conditions at low, mid, and high latitudes. Comparisons were made with 60 rocket temperature profiles, 14 rocket ozone profiles, 90 balloon ozone sondes, 13 H_2O balloon profiles, 7 NO_2 balloon profiles, and 14 HNO_3 balloon profiles. Further comparisons have been made with the Nimbus 7 Stratospheric and Mesospheric Sounder (SAMS) temperature results and the Solar Backscatter Ultraviolet (SBUV) ozone data. The results of the correlative measurement comparisons, accuracy calculations, and precision estimates are given in table 1. In all cases, the error bars for LIMS and correlative data overlap. Accuracies range from less than 2 K in temperature to 10 to 20 percent for gas mixing ratios. The measurement precision is about 0.4 K for temperature and 0.15 ppbv and 0.25 ppmv for constituents, depending on the channel. Details of the comparisons, descriptions of accuracy studies, and discussion of methods for estimating precision are presented in a series of LIMS validation papers (Remsberg et al. 1984; Russell et al. 1984a and 1984b; and Gille et al. 1984a and 1984b).

The inverted profile results from LIMS have been archived in tape form at the National Space Sciences Data Center (NSSDC), NASA Goddard Space Flight Center, Greenbelt, MD 20771. These tapes, called the LIMS Inverted Profile Archival Tapes (designated LAIPAT in the archive), contain profiles of temperature and mixing ratio at 38 latitude increments over the full altitude range for all days that LIMS was operating. A second archived product at

NSSDC is the LIMS Map Archival Tape (designated LAMAT in the archive). This product consists of calculations of the synoptic fields of the LIMS temperatures, mixing ratios of trace gas species, and geopotential heights, which were derived from the LAIPAT using a Kalman filter objective analysis mapping method (Rodgers 1976; and Kohri 1981). To study the propagation characteristics of planetary waves in the stratosphere and lower mesosphere, it is necessary to represent accurately not only the time mean state but also the time-varying wave motions of the temperature and geopotential height. Observed wave motions in the stratosphere are mainly planetary waves 1, 2, and 3. The appearance of this class of large-scale waves results from the selective filtering property of the upper atmosphere, which allows large-scale horizontal waves to propagate vertically while restricting the propagation of smaller scale waves. The temporal scales for these planetary waves range from about 1 to 4 weeks, and they should be easily detected with the LIMS sampling pattern. Another class of transient and global traveling planetary waves also exists in the stratosphere with periods of the order of several days. Resolution of this second class of waves requires a procedure for time interpolation of asynoptic satellite data. It will be shown that the Kalman filter technique represents an appropriate procedure for generating the desired synoptic fields. There are, of course, waves with an even shorter temporal scale. For example, the diurnal variation consists of a series of global waves traveling westward at the rate of one Earth revolution per day. For most areas of the globe the LIMS sampling pattern gives only limited information about these waves, and the Kalman filter process, as used for this analysis, gives no information about the synoptic structure of these diurnal waves. Some diurnal information can be obtained from the LAIPAT near terminator crossings. The LAMAT fields can be used for comparison with other synoptic fields and for calculating derived quantities, such as potential vorticity, wind fields, and eddy fluxes.

In generating the LAMAT, the LAIPAT data were linearly interpolated in logarithmic pressure coordinates to fixed standard pressure levels and mapped around latitude circles for the synoptic time of 12 noon Greenwich Mean Time (GMT). The mapped data are stored on the LAMAT in the form of 13 Fourier coefficients to represent the zonal mean and 6 zonal wave numbers as a function of latitude and pressure throughout the period of the LIMS mission. In some latitude or altitude ranges, missing data due to low signal-to-noise or cloud effects do not allow determination of all 13 coefficients. In these

cases lower wave number atmospheric features are discernible from the data.

This paper describes the general analysis procedure used in producing the LAMAT, and it discusses the quality of the temperature and derived geopotential height fields. Characteristics of the LAMAT data for the other LIMS species will be presented in two companion reports. Detailed comments about the LAMAT data and their format are given in the appendix.

Symbols

K	vector defined in equation (2)
<i>M</i>	order of the Fourier series, less than or equal to 6
<i>p</i>	pressure, mbar
S	error covariance matrix
<i>T</i>	temperature, K
<i>t</i>	time
<i>w</i>	weight factor (see eq. (14))
X	vector of Fourier coefficients
θ	latitude, deg
λ	longitude, deg
σ^2	variance
σ_{obs}	observed standard deviation between synoptic field and asynoptic data
ϕ	geopotential height, km
ϕ_{ref}	geopotential reference height (50 mbar), km

Subscripts:

avg	average (see eq. (12))
<i>e</i>	estimate
<i>F</i>	with increasing time (see eq. (12))
<i>L</i>	index of pressure level
<i>m</i>	measured
<i>n</i>	index of data points (see eq. (3))
<i>R</i>	with decreasing time (see eq. (12))
0	initial value

Superscript:

<i>T</i>	transpose
----------	-----------

Abbreviations:

GMT	Greenwich Mean Time
-----	---------------------

LAIPAT	LIMS Inverted Profile Archival Tape
LAMAT	LIMS Map Archival Tape
LIMS	Limb Infrared Monitor of the Stratosphere
NMC	National Meteorological Center
NOPS	Nimbus Observation Processing System
NSSDC	National Space Sciences Data Center

Analysis Procedure

Nimbus 7 Orbit and LIMS Data Set

Since the Nimbus 7 spacecraft was in a Sun-synchronous orbit, the track of the LIMS tangent point is a closed loop on a latitude versus local solar time grid (fig. 3). The track is divided into two segments, or nodes. The ascending node (node 1) is that part of the track where the tangent point is moving from south to north, and the descending node (node 2) is the rest of the track. The entire track, that is, node 1 plus node 2, is called the combined node (node 3). The second curve in figure 3 shows the location of the boundary between daylight and darkness, that is, the terminator, on December 21 at an altitude of 30 km. If one starts at the extreme southern end of the track and follows the ascending node northward, the measurements for the map analysis are selected from the LAIPAT at approximately 4° intervals in latitude from 64°S to 83.5°N. Each measurement is taken within 1° of the desired latitude. The same procedure is followed on the descending node. The period of the orbit is about 104 minutes; thus the measurements for either node 1 or node 2 at a specific latitude compose a time series with points taken every 104 minutes. This sequence of measurements is taken at the same local solar time, but the longitude of each measurement is 26°W of the location of the previous measurement; of course, data gaps occur occasionally. Note that in general the ascending and the descending node measurements are in daylight and in dark, respectively. Near solstice both nodes occur in daylight or in dark close to the poles.

The Nimbus 7 orbit imposes two basic limitations on the use of these data to calculate a synoptic map. First, there are at most 28 measurements, 14 each for nodes 1 and 2, at a given latitude per day. This limits the number of horizontal wavelengths that can be resolved. In addition, for node 1 or 2 these measurements are taken at only one local solar time. If the combined node is used, the measurements occur at two local solar times. The implications of

this sampling pattern will be discussed later when the results of the analysis are described.

Calculation of Synoptic Fields

The synoptic fields can be represented by a set of Fourier coefficients calculated for noon GMT for each of the three nodes and at each latitude and pressure level (4° latitude increments and 18 atmospheric pressure levels). The temperature field T at a particular time (GMT) t , latitude θ , and pressure p is given in vector form by

$$T_{t,\theta,p}(\lambda) = \mathbf{K}^T(\lambda) \cdot \mathbf{X}_{t,\theta,p} \quad (1)$$

where

$$\mathbf{K}^T(\lambda) = [1 \cos \lambda \sin \lambda \cos 2\lambda \dots \sin M\lambda] \quad (2)$$

λ	longitude
M	the order of the Fourier series, less than or equal to 6
\mathbf{X}	the vector of Fourier coefficients X_j ($j = 1, 2, \dots, M + 1$)

and the superscript denotes the transpose of a vector.

For the rest of this paper the subscripts θ , t , and p will be understood. Synoptic data (or "snapshots" of global parameters) are required to calculate \mathbf{X} in equation (1) exactly. However, the discrete form of equation (1) is actually used to solve for \mathbf{X} :

$$T_n = \mathbf{K}_n^T \cdot \mathbf{X}_n \quad (3)$$

where T_n is the measured value of the field at time t_n and longitude λ_n .

One way to find \mathbf{X} is to take the data for some time period, for example, 1 day, and, neglecting any time variations within that period, perform a least squares minimization on equation (1) to find the best mean value for \mathbf{X} for that day. Instead of using this approach however, we have chosen a Kalman filter technique, which is considerably different in that a best fit field for a particular time was sought rather than a mean field for some time period (Rodgers 1976; and Kohri 1981). This approach is well suited to handling the LIMS data, since the instrument was turned off for whole orbits or even for a whole day.

Kalman Filter

The Kalman filter can be thought of as a sequential estimator. It is assumed that an initial estimate of the field is available, and that estimate is updated by the assimilation of each measurement in

the data time series. Calculation of the initial field is described later. Inherent in the use of the Kalman filter is the assumption that an estimate exists of both the uncertainty in the input data and the rate of increase of the uncertainty involved in the field. Since all the measurements T_n that were used to calculate the field \mathbf{X}_n involve some error (assumed to be random), there must be an uncertainty associated with \mathbf{X}_n , represented by an error covariance matrix \mathbf{S}_n . If equation (3) is used to calculate the temperature field at λ_n and t_n , then the uncertainty, or variance, associated with this estimate is

$$\sigma_n^2 = \mathbf{K}_n^T \mathbf{S}_n \mathbf{K}_n \quad (4)$$

When \mathbf{X}_n is used to estimate the field at times other than t_n , the error covariance matrix must be increased by an amount $(d\mathbf{S}/dt)\Delta t$. For now it is assumed that $d\mathbf{S}/dt$ and $d\mathbf{X}/dt$ are known. Later, the calculation of these terms is described. Since estimates of \mathbf{X}_{n-1} and \mathbf{S}_{n-1} are known from the previous time step, it is possible to estimate these terms at t_n by using

$$\mathbf{X}_{n,e} = \mathbf{X}_{n-1} + (t_n - t_{n-1})d\mathbf{X}/dt \quad (5)$$

and

$$\mathbf{S}_{n,e} = \mathbf{S}_{n-1} + |t_n - t_{n-1}| d\mathbf{S}/dt \quad (6)$$

where the absolute value of the time difference is taken because the uncertainty in the estimated value increases with absolute time difference since its last determination.

These expressions can then be used to estimate the measurement at t_n , that is, $T_{n,e}$ (from eq. (3)), and the variance of that estimate, that is, $\sigma_{n,e}^2$ (from eq. (4)). This process is illustrated in figure 4. The values T_{n-1} and σ_{n-1}^2 are known at time t_{n-1} . Equations (3), (4), (5), and (6) are used to estimate $T_{n,e}$ and $\sigma_{n,e}^2$. The estimate $T_{n,e}$ is combined with the actual measured temperature at t_n ($T_{n,m}$) using the variances ($\sigma_{n,e}^2$ and $\sigma_{n,m}^2$) as weighting factors. The Kalman filter equations, as they have been applied in the LIMS LAMAT processing, are

$$\mathbf{X}_n = \mathbf{X}_{n,e} + \frac{\mathbf{S}_{n,e} \mathbf{K}_n (T_{n,m} - T_{n,e})}{\sigma_{n,e}^2 + \sigma_{n,m}^2} \quad (7)$$

$$\mathbf{S}_n = \mathbf{S}_{n,e} - \frac{\mathbf{S}_{n,e} \mathbf{K}_n \mathbf{K}_n^T \mathbf{S}_{n,e}}{\sigma_{n,e}^2 + \sigma_{n,m}^2} \quad (8)$$

which can be used in equations (3) and (4) to obtain new estimates of the field T_n and its uncertainty σ_n^2 . On the basis of these estimates, the procedure can be repeated to obtain T_{n+1} and σ_{n+1}^2 . The details

of this procedure are described in Rodgers (1976 and 1977) and Kohri (1981).

Note that the estimated and measured fields and their variances play equivalent roles in equations (7) and (8). In fact, there are two sets of data involved in this analysis. The first set is just the measured quantities ($T_{n,m}$, λ_n , and t_n). The second set contains estimated, or virtual, quantities ($\sigma_{n,m}^2$, $d\mathbf{X}/dt$, and $d\mathbf{S}/dt$). The selection of reasonable virtual data is necessary to the operation of the filter, and this process is described in the following section.

The first step in applying the Kalman filter was to choose the order of the Fourier series. This was done by considering the number of data points per day at each latitude and then calculating the order M from the relation

$$M = \frac{\text{Number of points/day} - 1}{2}$$

In no case was M greater than 6 for node 3 or greater than 4 for nodes 1 and 2. In some cases this limitation on the order of the Fourier series results in a map that has different wave resolution at different latitudes. Also the number of waves at a latitude can change from one day to the next; however this occurs only on days processed by different Kalman filter runs. See the appendix on the format of the LAMAT for a description of how to determine the wave resolution.

The next step in applying the Kalman filter during the LAMAT processing was to estimate an initial field \mathbf{X}_0 , and an initial covariance matrix \mathbf{S}_0 . This was done by using one measured data point at a time to calculate the field and error covariance matrix at t_n using equations (5) and (6).

From equation (7) one can see that the new value of the field \mathbf{X}_n is just a linear combination of both the estimated field $\mathbf{X}_{n,e}$ and a term that depends on the difference between the measurement $T_{n,m}$ and its estimated value $T_{n,e}$. The factor multiplying this difference is the Kalman gain vector. This vector operates on $(T_{n,m} - T_{n,e})$ to partition this difference between the components of \mathbf{X}_n . The partitioning depends not only on the longitude and the time since the last measurement but also on the uncertainty of the various elements of \mathbf{X}_n . In general, a greater uncertainty in an element of \mathbf{X}_n leads to a greater change in \mathbf{X}_n during the next time step. Of course, similar comments apply to \mathbf{S} . The process of averaging the measured data and obtaining the estimated value is clearer if equation (7) is premultiplied by \mathbf{K}_n^T

in equation (3) to yield

$$T_n = T_{n,e} + \frac{(T_{n,m} - T_{n,e})\sigma_{n,e}^2}{\sigma_{n,e}^2 + \sigma_{n,m}^2} \quad (9)$$

By both premultiplying and postmultiplying equation (8) by \mathbf{K}_n^T and \mathbf{K}_n , respectively, one obtains after algebraic manipulation

$$(\sigma_n^2)^{-1} = (\sigma_{n,e}^2)^{-1} + (\sigma_{n,m}^2)^{-1} \quad (10)$$

Note that the variance after the update σ_n^2 is always less than either the estimated variance or the variance of the measured data. Given a measurement $T_{n,m}$ and the estimate $T_{n,e}$, the value T_n represents a better estimate of the field than either $T_{n,e}$ or $T_{n,m}$, just as \mathbf{X}_n represents the best estimate of the field based on the history of both the data and the assumed virtual data.

There are two special cases of equations (9) and (10) that are important to the processing of the LIMS data. Consider what happens when $d\mathbf{S}/dt$ is very large. Then $\sigma_{n,e} \gg \sigma_{n,m}$ and in the limit

$$T_n = T_{n,m} \quad \sigma_n^2 = \sigma_{n,m}^2 \quad (11)$$

so that each data point is fit *almost* perfectly. It may seem that in this case all information from the previous estimate \mathbf{X}_{n-1} has been lost, but this is not true. The coefficients of \mathbf{X}_{n-1} have been changed, but unless \mathbf{X} has only one coefficient, the effect of the previous measurements is still present in \mathbf{X}_n . For a greater number of coefficients in \mathbf{X} , more data must be inserted before the effects of past data are eliminated. Thus, there is an inherent time smoothing in the development of \mathbf{X} that is a function of the number of coefficients in \mathbf{X} as well as the time spacing between the measurements. Of course, when $\sigma_{n,e}^2$ is much greater than $\sigma_{n,m}^2$, additional time smoothing is introduced because of the averaging of $T_{n,m}$ and $T_{n,e}$. The second special case occurs when \mathbf{X} must be calculated at a time for which there is no data point. In this case it is assumed that a value exists at that time, but that its variance is infinite. Equations (7) and (8) yield

$$\mathbf{X}_n = \mathbf{X}_{n,e} \quad \mathbf{S}_n = \mathbf{S}_{n,e}$$

The factor $\sigma_{n,e}^2/(\sigma_{n,e}^2 + \sigma_{n,m}^2)$, in equation (9), is the update factor. It is the fractional part of the difference between the estimated and the actual measured value that is used to update the estimate of the field. This factor determines how quickly the filter responds to differences between the measurement and the estimate.

As to this point, processing of the data has been described only for $t_n > t_{n-1}$, that is, for time increasing. When \mathbf{X} is evaluated at some given time, it depends only on data taken at or before that time, and since the filter is smoothing the field, the calculated field will lag behind the true value. To overcome this feature and improve the estimate, the data can also be processed in reverse time order; thus, the absolute value of the time difference is used in equation (6). When this reversed processing is done, a second estimate of \mathbf{X} is developed that depends only on data taken at later times. Each of these estimates has an associated error covariance matrix. A final estimate of the field can be calculated by averaging the forward and reverse estimates, \mathbf{X}_F and \mathbf{X}_R , using the corresponding error covariance matrix \mathbf{S}_F and \mathbf{S}_R , as weighting factors. Thus, the best estimate of the field is

$$\mathbf{X}_{\text{avg}} = \mathbf{S}_{FR}(\mathbf{S}_F^{-1}\mathbf{X}_F + \mathbf{S}_R^{-1}\mathbf{X}_R) \quad (12)$$

where

$$\mathbf{S}_{FR} = (\mathbf{S}_F^{-1} + \mathbf{S}_R^{-1})^{-1}$$

This final estimate at time t then depends on the data taken both before and after time t .

The Virtual Data Set

Evaluation of the elements of the virtual data set ($\sigma_{n,m}^2$, $d\mathbf{S}/dt$, and $d\mathbf{X}/dt$) is discussed in this section. Proper selection of these elements is necessary to the successful application of the filter since they determine the degree of smoothing in the filter process.

The variance of the data $\sigma_{n,m}^2$ can be described most easily. Initially, variance may be thought of as the measurement precision of the data (expressed as a variance). Such initial estimates of precision were taken from the LIMS validation papers (see, for example, table 1). However, those estimates, which were made by comparing adjacent vertical profile scans, serve only as a first estimate of the precision (low value of variance). Several other effects must be included. For example, the LAIPAT data were processed for specified latitudes but were actually within 1° of each latitude circle. These data were used as if they were directly on the required latitude; that is, they were not interpolated to estimate the value at the exact latitude. Thus, in regions of strong latitudinal gradients there may be errors introduced by the lack of precision in latitude. In addition, $\sigma_{n,m}^2$ was used to account for shortcomings in the model. For example, in some regions some time smoothing was employed to obtain more reasonable agreement between the input and output statistics of the filter. This was accomplished by increasing $\sigma_{n,m}^2$, and this

parameter was the only control for the filter output during the processing. (This procedure will be discussed in detail in the section describing the analysis of the filter output.) The final result is that $\sigma_{n,m}^2$ was taken to be as small as possible (but never smaller than the first estimate of the precision), while being consistent with statistics obtained from both the input and the output of the filter. The set of $\sigma_{n,m}^2$ for temperature for the January–February period is shown in table 2. These values varied somewhat with season because they were based on precision estimates from the profile data, which contain variations due to real atmospheric motions in addition to the instrumental and data retrieval uncertainties.

Next consider the term $d\mathbf{S}/dt$, which corresponds to the $\Delta\mathbf{S}$ in Kohri (1981). Kohri defined $d\mathbf{S}/dt = \mathbf{S}_{\text{clim}}/\tau$, where \mathbf{S}_{clim} is the climatological covariance matrix of the observed temperature field and τ was set to 3.7 days. He limited \mathbf{S}_{clim} to a diagonal matrix. For each of the zonal waves in the model he calculated the variance of the i th wave amplitude $\sigma_{A,i}^2$. This variance was then divided equally between the sine and cosine coefficients of that wave component. Thus, the element in the 4th row and column of $d\mathbf{S}/dt$ would be

$$\sigma_{\text{clim},2}^2/(2 \times 3.7)$$

where $\sigma_{\text{clim},2}^2$ is the climatological variance of wave 2.

In the present analysis, Kohri's procedure had to be modified because appropriate preexisting data for many of the LIMS parameters were not available to calculate $d\mathbf{S}/dt$. In addition, it was desirable to allow for a variable τ and to include the term $d\mathbf{X}/dt$. In order to meet these needs, it was necessary to obtain estimates for the data fields and thereby obtain a means to estimate the virtual data. This was done by using the Kalman filter to make a preliminary estimate of the field. This preliminary estimate assumed that $d\mathbf{S}/dt$ was very large and independent of wave number. Thus, these preliminary fields were produced with minimal smoothing and are in fact only somewhat smoother than would have been obtained with a simple least squares fit to the data. Output from the preliminary run was treated as if it were atmospheric data and was used to calculate the virtual data set. The output was analyzed to obtain the first time derivative of the zonal mean coefficient, $d\mathbf{X}_1/dt$; all other elements of $d\mathbf{X}/dt$ were set to zero. The slope, $d\mathbf{X}_1/dt$, was removed from the data, and then the resultant data were used to calculate the variance of the amplitudes of the waves and the zonal mean. The autocorrelation of each wave amplitude at each latitude was also calculated, and the time

for the autocorrelation to reach the noise level was found. This relaxation time was then averaged for all latitudes to obtain the mean relaxation time (τ) (see table 3, for example). However, τ was never set to less than 1 day. Because of values assumed for the virtual data set, the results of the preliminary filter run show a larger variation from day to day than was expected and the influence of spurious data can be significant. Thus, the output from these runs was carefully checked to remove the effects of obviously incorrect data. As expected, $d\mathbf{S}/dt$ calculated from these runs have larger values than those found in the final filter runs since each subsequent filter run serves to smooth the output. It seemed prudent to use variances that may be slightly overestimated by the approach herein, rather than choosing lower bound uncertainties for the data in the filter analyses. The final Kalman filter run introduced some minimal smoothing to the data.

General Analysis of the Kalman Filter Output

The task of analyzing the fields produced by the filter was the most difficult and time-consuming part of producing the LAMAT product. To appreciate the magnitude of this problem and to understand why the analysis described herein was used, consider the number of maps contained in this data set. There are 18 pressure levels for temperature and O_3 , 12 levels for H_2O and NO_2 , and 10 levels for HNO_3 . For temperature and O_3 , H_2O , and HNO_3 , there are maps for all three nodes, and for NO_2 , maps for nodes 1 and 2. Geopotential height fields on the LAMAT are calculated at 18 pressure levels from the node 3 LAMAT temperatures and a reference geopotential height. Note that this updated description of the LAMAT differs from that in table 3 of Gille and Russell (1984). There are data for 212 days. Thus, there are 45 792 individual maps in this data set. Since the maps consist of coefficients at 38 latitudes, there are nearly 1.74×10^6 sets of Fourier coefficients \mathbf{X} , and it was not possible to examine each set individually.

The approximate vertical spacing of the 18 temperature levels on the LAMAT varies from 2.3 to 4.3 km depending on the level, whereas the point spacing on the LAIPAT is 1.5 km. The vertical interpolation procedure incurs a smoothing of small-scale structure, and amplitudes of vertical waves that were resolvable on the LAIPAT are, on average, reduced somewhat in the LAMAT preparation. The amount of the amplitude reduction for a wave on the LAMAT depends on its vertical wavelength and the original emissivity weighting functions for the

CO₂ channel radiance profile for the given atmospheric state. Waves with half-wavelengths shorter than 3.5 to 6.5 km (corresponding to vertical level spacing) are not sampled adequately in the LAMAT and their characteristics are aliased to longer wavelengths.

The principal difficulty in analyzing the filter output was lack of definite criteria with which to judge the fields. The approach adopted was to develop a set of criteria, and if the results satisfied these general, and sometimes intuitive, criteria, they were accepted as being "good." These criteria are outlined here with added discussion in the sections on the individual parameters.

It might seem that the simple criterion of how well the data fit the calculated field would describe the quality of the mapped field. However, such an approach requires a solid understanding of the uncertainties involved in both the data and the model. Such a detailed analysis of this data set, given the limited time and resources available, was not feasible. An approximation was therefore used to estimate the quality of the field. From the fields produced at noon GMT, a parameter value (e.g., temperature) was calculated at each longitude for which there was a measurement for that day. The standard deviation between the measurements and the results calculated from the field was determined. Thus, this standard deviation is the measure of the fit between the estimated noon time field and all data taken within 12 hours of that time. If the measured field was stationary and the model was adequate, this standard deviation should be near $\sigma_{n,m}^2$. On the other hand, if the measured field was transient or not well represented by the model, then the calculated standard deviation should be greater than $\sigma_{n,m}^2$. The calculated standard deviations have been included on the LAMAT so that the user can judge the quality. The user should keep in mind the limitations of this quantity and remember that it is an indication of the fit between the estimate of the synoptic field and the synoptic measurements. A poor fit may indicate poor results, poor data, or simply a period of rapid variation in the fields. This quantity should not be taken as proof of "bad" results.

Another qualitative test of the LAMAT product is a comparison of the fields produced for both the ascending and the descending node. If these fields agree for parameters that are not expected to have significant diurnal variations, it provides confidence in both the Kalman filter results and the data. If on the other hand, they do not agree and if the user cannot attribute the difference to a true diurnal variation or an indicated variation in the measurements, then one must question the results of at least one

of the nodes. Certainly the combined node results would be in doubt.

Except for the initial estimate of the field, the Kalman filter processing was not coupled in any way with latitude or pressure. Thus it is reasonable to use the continuity of \mathbf{X} with latitude and pressure as another measure of the quality of the Kalman filter results. The existence of continuity is certainly an indication of good results; however, as will be shown when discussing certain data, the presence of sharp gradients in latitude or pressure does not suggest or prove the results bad, especially for high winter latitudes. A final check was a comparison of maps on a pressure surface for a series of days to see whether the prominent features in the map changed in a reasonable way and whether they seemed to correspond to prominent features in the maps of other species.

If the results from one of the filter runs seemed to fail one of the above tests, the data were examined to determine whether there was any apparent difficulty. If one was found, the analysis was repeated with adjusted $\sigma_{n,m}^2$ before it was accepted. At no time were the results of a run altered just to remove a questionable feature. Instead, every effort was made to base the map analysis on the data that went into producing the maps, not on some preconceived idea of how the maps should appear.

Processing for the LAMAT

Several data processing steps were required before the LAIPAT profiles were input to the Kalman filter software. LAIPAT profiles were read and retained only if the data were defined as good by the header indices for each scan and each of the five LIMS parameters. The header contains "flags" to identify problems such as obviously noisy data or partial inversions. Segments of scans that contained cloud-contaminated data were also eliminated. Data affected by polar stratospheric clouds (PSC's) were retained and those situations were handled somewhat empirically, as described below. The remaining good data were linearly interpolated (in logarithmic pressure) to the standard pressure levels used in the LAMAT processing. Finally, the data were sorted according to latitude.

An additional check was made during each Kalman filter run to eliminate obviously spurious data. This was first done by eliminating data that were obviously too large or too small. For example, the limits on temperature were set to 320 K and 180 K. Any point that was rejected by these limits was checked. Less than 0.01 percent of the data were removed this way. In addition, the filter was used to remove data that were grossly inconsistent with

the surrounding data. This was done by comparing $T_{n,m} - T_{n,e}$, in equation (7), with its mean standard deviation. If at any time $T_{n,m} - T_{n,e}$ exceeded a 5-sigma criterion, then that measurement was not used to calculate a new \mathbf{X}_n . Less than 0.05 percent of all temperature profiles were excluded by this screening criterion. Usually the need for screening was traced to poor pressure-altitude registration or rapidly varying atmospheric gradients. Particularly strong horizontal and vertical temperature gradients occurred between 60°N and 84°N during January 21–23 and February 6–11, but even in those instances, very few profiles were removed. Therefore, mapped fields prepared even for those periods are considered accurate.

The effects of PSC's (McCormick et al. 1982) could be clearly seen in the LIMS data at high latitudes in the lower stratosphere. They were apparent in the ozone and water vapor data at high northern latitudes on many days in January, and at some times and pressure levels, they occupied as much as 17 percent of the polar cap north of 60°N. Because these spurious data would result in serious errors in the map coefficients, it was decided to remove all data that could be attributed to PSC's. The procedure used to remove these data relied on inspection of the preliminary ozone maps. Thus temperature profile segments that could have been affected were deleted during the LAMAT processing, even though there was no noticeable effect on radiances in the wide CO₂ channel used for retrieving temperature. This deletion means that the LAMAT temperatures at a given latitude are being extrapolated across sectors where data were deleted. The Kalman filter estimate of the temperature, where the profile segments were deleted, can be either too warm or too cool, depending on the distribution of the temperatures over the region where data were not deleted. Differences have been calculated between the temperature fields both with and without the "contaminated" segments. Zonal mean differences at 30 mbar are less than 0.5 K with maximum differences at any given longitude being less than 4.3 K, but on the average less than 2 K.

The processing for the LAMAT can be summarized as follows:

1. Vertically interpolate, sort, and reformat the LAIPAT data.
2. Make the preliminary Kalman filter run covering 30 days and large $d\mathbf{S}/dt$.
3. Use the output of step 2 to
 - a. Remove polar stratospheric clouds.
 - b. Calculate $d\mathbf{X}/dt$.
 - c. Calculate σ_{clim}^2 by wave number and latitude.
 - d. Calculate the relaxation time by wave number.

4. Estimate $\sigma_{n,m}^2$.
5. Make a new Kalman filter run using results of steps 3 and 4, parameter limits, and 5-sigma criterion.
6. Analyze the results of step 5 to
 - a. Check rejected data, observed standard deviations σ_{obs} , and calculated σ_{clim}^2 . Do the results look "reasonable"?
 - b. Check latitude and pressure continuity.
7. If necessary go back to step 4 and repeat the sequence with adjusted values of $\sigma_{n,m}^2$. If the case is rerun, is it better or worse? If necessary, reevaluate data analysis procedure (step 3).
8. Combine the final results of all pressure levels, nodes, and species for one period onto an LAMAT.

Temperature Maps

The first question often raised about the maps is, "How well do they fit the data?" Recall that the LIMS coefficients can be used to calculate synoptic maps for noon GMT and, as such, are not intended to fit the asynoptic data from which they were derived. In spite of the limitations involved with comparing the asynoptic data with the synoptic maps, extensive use of this difference diagnostic is made in analyzing the results of the filter processing. An example of this comparison is shown for temperature in figure 5 for 60°N at 30 mbar on January 26. The symbols show the asynoptic data for all three nodes for this date and latitude. The symbols with the plus (+) sign indicate the first point for this date and for a given node. The time of day in hours since midnight GMT is given in the figure. For example, in figure 5, the first data points for the ascending and descending nodes were taken at 02:36 and 02:54, respectively. Thus, the time sequence of data for one node starts at that longitude and moves westward at about 26° per orbit. The curves, which are the noon GMT estimates of the temperature field, fit the overall variations of the data. It is important to recognize that there is a measurement effect from the periods both before and after this date and that it influences the curves shown for this day. Examination of such data sequences is useful for understanding why the fields are as shown. In this case, the fact that the measurements for nodes 1 and 2 are quite close together in longitude, even though they are separated by almost 9 hours, indicates that the observed field is rather steady for this day and helps explain the good fit between curves and data. The standard deviation between the data and the calculated field is shown on the figure. This calculation assumes that there was no variation of the field during the day.

The effect of a large time variation on this type of plot is shown in figure 6, where data for all three nodes for 83.5°N at 5 mbar are shown for February 3, 4, and 5. Again the plus (+) sign denotes the first data point in the day. During this period an atmospheric warming occurs and the temperature at each longitude is increasing rapidly. Because the track of the tangent point is near 70°E at noon GMT, the data fit the derived field best in this region. This does not mean that the derived field is poor near 250°E; it only means that the data taken there is for a time 12 hours earlier (or later) than the time for which the map is produced. If a map were produced for midnight, the data would be fit best in the region of 250°E. However, if a plot were developed for midnight, the data represented by each set of symbols should be taken within 12 hours of midnight, not of noon, and the discontinuity would appear near 70°E rather than at 250°E as shown. Figure 6 clearly illustrates the shortcomings of using the fit between the map and the data for only one day for judging the quality of the map. The large standard deviation of 3.3 K or greater is due, in part, to the rapid time variations of the temperature.

Another possible cause of large observed standard deviations (σ_{obs}) between the data and the LAMAT curves is illustrated in figure 7. These data, for the Equator at 0.7 mbar on February 23, display a significant difference between day and night, possibly due to tides (Hitchman and Leovy 1985). The standard deviations for the node 1 and 2 curves are 1.46 K and 3.55 K, respectively (much of the difference in the node 2 data is due to only a couple of points). For the combined node map the standard deviation is 5.37 K. Combined node maps for such situations should not be used; the user should recognize that there is a day-night difference and that the nature of the LIMS sampling pattern usually gives only limited information about a diurnal cycle. At any rate such a cycle is not considered in the field model of the filter (eq. (1)), so that a significant diurnal variation is likely to invalidate any results obtained with the combined node data set.

Figure 8 illustrates the responsiveness of the Kalman filter to traveling waves. The data distribution for a pressure level of 10 mbar near 60°N during December was used to model a westward traveling wave 1 transient. The actual data for this period were replaced by a field with a zonal mean of 210 K and a 10-K amplitude traveling wave (westward). The phase velocity was varied from 1 cycle/day to 16 cycles/day. The zonal mean and wave 1 amplitudes calculated from the Kalman filter are shown in figure 8. The calculation of the zonal mean is very accurate except for periods near 1 day (fig. 8(a)). This

error near the 1-day period results from the satellite and the wave being in phase. Thus instead of sampling the entire wave, the satellite samples only one value in its cycle. When the phase speeds of the satellite and the wave differ only slightly, it takes a long time for the entire range of the wave to be sampled. The calculated amplitude of wave 1 is shown in figure 8(b). Again the satellite does not detect a wave at 1 cycle/day (westward). The one value of the wave that is being sampled is seen as a zonal mean term and differs for the two nodes. As the phase speed decreases, the filter begins to respond; however, it interprets the one wave as a combination of all waves. The slower the wave travels, the better the amplitude of the wave is recovered. The observed standard deviation is shown as the dotted curve in figure 8(b). It is zero for the phase speed of 1 day, increases sharply, and then decreases with decreasing phase speed. The assumed standard deviation of the data was 0.9 K. If this had been actual data being processed, the quality of the fit would have been judged good at a standard deviation of less than 2 K. It is clear from this illustration that the LAMAT data cannot detect diurnal variations by looking at only one node. Some diurnal information can be recovered by comparing nodes 1 and 2; however, this must be done very carefully. There is never any diurnal information in node 3. The amount of data on hand, the sampling pattern, and the response time of the filter combine to prevent the recovery of this information in only one node.

Figure 9 shows a situation where the large standard deviations are not explained by either asymptotic sampling or diurnal variations. At 52°N and 1 mbar on December 14, the ascending node data show a series of large variations that produce a standard deviation of 7.24 K. The descending node yields a better fit but still has an error of 4.48 K. The combined node presents a very poor fit to the data, especially in the region of 120° to 270°E, but this is a direct result of the large differences in the data in this region. The LIMS LAIPAT data have been examined for this period to determine whether there was anything odd about the retrievals or the horizontal temperature gradients applied during the retrieval (see Gille et al. 1984a). Consecutive profiles obtained along orbits exhibited no discontinuous changes which would indicate a retrieval problem, and the calculated spacecraft motions were not anomalously large. In view of the obvious limitations of the standard deviation criteria for assessing LAMAT data quality, it is important that the researcher use them as they were intended, that is, not as proof of good or bad results, but as an indicator of regions of poor fit between the asymptotic data and the synoptic map.

The general distribution of σ_{obs} is illustrated in figure 10, which shows the monthly mean values for the ascending node for January and May. In both cases the minimum value of σ_{obs} is in the lower summer stratosphere. The magnitude increases toward the winter hemisphere and with increasing height. The increase with height is, at least in part, related to the reduced signal-to-noise ratio at lower pressures, while the increase toward the winter hemisphere results from increased wave activity and the presence of larger zonal mean gradients in these regions. The minimum values of σ_{obs} , 0.6 and 0.3 K in January and May, respectively, are consistent with the estimated precision of the temperatures (Gille et al. 1984a).

The monthly mean values of the zonal mean temperature for January and May are shown in figure 11, and the corresponding monthly mean standard deviation of the daily temperature from the zonal mean is given in figure 12. Note that for both months the regions of large σ_{obs} in figure 10 are closely correlated with the regions of large wave amplitude in figure 12. Thus the larger σ_{obs} in this region illustrates the effects of the wave transience and the limitations, previously discussed, of the calculation of σ_{obs} .

The differences between the monthly means of the ascending and descending node zonal mean temperatures for January and for May are shown in figure 13. Recall that the zonal mean coefficients for these nodes are the results of measurements made at only one local time. Thus, a diurnal wave will travel with the satellite and will always be sampled at the same position relative to its nodal points and will appear as a constant field, not as a wave. Hitchman and Leovy (1985) have analyzed the differences in ascending and descending node zonal means from the LAMAT and related them to tidal effects. Clearly, the differences in these zonal means are due to wave effects that are appearing in the zonal mean coefficients because of the LIMS sampling pattern.

A further quality check of the LAMAT was conducted by examining the consistency between maps of the three nodes. Because each latitude-pressure combination was processed independently, any lack of continuity becomes a concern. Figure 14 presents amplitudes and phases (longitude of the maximum) of the zonal mean and waves 1 through 4 as a function of latitude for a pressure level of 3 mbar on February 26. Once again the zonal mean term (fig. 14(a)) clearly shows the day-night differences near the Equator. Where such zonal mean differences are small, the remaining plots can be used to estimate the "noise" level in each component of the field. Amplitude plots are straightforward, while the phase plots are meaningful only when the wave am-

plitudes are well above the repeatability of the temperature data (which is about 0.7 K at 3 mbar (Gille et al. (1984a))).

Amplitudes of the zonal mean and waves 1 through 4 are displayed for the 10-mbar level at 64°S in figure 15 for a period of 31 days beginning October 25. Because of the time smoothing by the Kalman filter, curves in figure 15 are not as noisy as those in figure 14, where no comparable smoothing was attempted to reduce noise in the meridional direction. As with figure 14, plots like those in figure 15 were used to identify problems in the data or the filtering process, but such instances were rare.

During late January and February of 1979 there was a series of sudden warmings in the Northern Hemisphere (Quiroz 1979). Figure 16 presents the amplitudes of the zonal mean and waves 1 through 4 for each node at 83.5°N and 10 mbar for the month of February. The zonal mean temperature increases by nearly 40 K from February 3 to 7, yet the values calculated for the three nodes are very close. The wave 1 amplitude increases from 2 K to 20 K. Wave 2 also increases, but reaches its maximum amplitude at 83.5°N several days later. The phases (not shown) agree closely for all nodes for waves 1, 2, and 3.

Polar stereographic maps of temperature are shown in figure 17 for February 1, 5, and 9 at 10 mbar in the Northern Hemisphere. These data show the rapid temperature changes that are measured. Initially there is a large wave 1 and 2 signature located at 68°N with a sharp meridional gradient poleward of the high around 60°E. The region of high temperature near 70°E moves eastward and poleward during succeeding days, causing the region of large gradients to be swept across the 83.5°N latitude and leading to the rapid temperature rise in figure 16. Similar variations occur in figure 6 at the 5 mbar level for February 3.

To summarize the quality of the LAMAT temperatures, the following points are stressed. Results for the lower stratosphere, 10 to 100 mbar, generally agreed with the input data to within the precision of the retrieved temperatures. At pressure levels above this region, there may be some degradation as defined by the standard deviation of the differences between the filter results and the data. In most instances the amplitudes of waves 5 and 6 are near the noise level or are unreliable because of the rapid variations that they undergo. Regions of strong day-night differences (5 K) occur in the lower subtropical mesosphere, and node 3 maps should be interpreted with this in mind.

It is recommended that if the data are to be used on isentropic surfaces, then the Kalman filter processing should be performed on these surfaces. This approach has several advantages. First, it

makes use of the high vertical resolution of the LIMS data, thus avoiding an unnecessary interpolation over large pressure increments. Second, the fields on the isentropic surfaces often show less variation than on the pressure surface, thus making the task of the filter easier. But most important, the interpretation of the meaning of the filter output is simpler, in that the physics of the transport process is more straightforward on these surfaces. Since much of the difficulty encountered in producing the maps was in determining their physical significance, the use of isentropic surfaces would be an appropriate aid to producing good Kalman-filtered maps.

Geopotential Height Fields

The geopotential height results were obtained using LIMS LAMAT temperature data, in combination with a National Meteorological Center (NMC) reference base level. Only node 3 temperature results were used in constructing the height fields and no smoothing of temperature with latitude was performed prior to the calculations. In general, the Kalman-filtered synoptic temperature estimates were available in Fourier coefficient form through degree six. In some instances, at pressure levels of 100 and 70 mbar in the tropics and 0.05 mbar at high latitudes, there were insufficient temperature data to resolve six zonal waves. In these cases, the shorter wavelength temperature coefficients were set to zero (i.e., not calculated) and were used as such in the height field calculations, which were always performed through degree six. There are no flags in the LAMAT geopotential height data to inform the researcher when the higher degree coefficients are affected. Because the 50-mbar level is the reference geopotential level, uncertainties in temperature at, say, 70 mbar were not integrated vertically to higher altitudes.

NMC data at the 50-mbar reference pressure level were obtained from special Nimbus Observation Processing System (NOPS) tapes and were presented in fields of 4225 grid points in a 65×65 array for both the Northern and the Southern Hemisphere. The data, which were packed in a format described in NMC Office Note 84, had a grid increment of 381 km at 60° latitude and a time tag of noon GMT. A bicubic spline technique (Greville 1967) was utilized for interpolation for each hemisphere from the NMC grid system to one compatible with the LIMS data reduction values, that is, 5° longitude increments and 4° latitude increments extending from 64°S to 83.5°N . A least squares technique was then used to reduce these grid data to Fourier coefficients (degree 6) for each specified latitude value. Because

each hemisphere was analyzed separately, discontinuities across the Equator (about 30 meters or less) are observed there in the 50-mbar heights. Reference heights at the Equator were used from the interpolated Northern Hemisphere fields only, because the Southern Hemisphere reference height fields often displayed discontinuous features in time and longitude at low latitudes.

For those isolated days when NMC data were not available (see table 4), the reference height values were obtained by interpolation between adjacent days about the missing data. On rare occasions, a zero value was calculated for a coefficient at 50 mbar on those missing days (see appendix on LAMAT format).

The geopotential height results were calculated from

$$\phi_L = \phi_{\text{ref}} + \sum_{n=1}^L \Delta\phi_n \quad (13)$$

where ϕ_L is the height at some pressure level, p_L , ϕ_{ref} is the reference base level, and $\Delta\phi_n$ is the thickness between specified pressure levels obtained from vertical integration of the temperature data. A total of 18 pressure levels, ranging from 100 to 0.05 mbar, were utilized. Straight line numerical integration techniques were used for the thickness calculations. Thus,

$$\phi_L = \phi_{\text{ref}} + (R/2) \sum_{n=1}^L w_n T_n \quad (14)$$

where T_n is the Fourier coefficient representation of the LIMS temperature data at pressure p_n , R (m/K) is a constant (287/9.81), and

$$w_n = \begin{cases} \ln(p_{n-1}/p_{n+1}) & (2 \leq n \leq L-1) \\ \ln(p_n/p_{n+1}) & (n=1) \\ \ln(p_{n-1}/p_L) & (n=L) \end{cases}$$

The quality of dynamical quantities derived from the LIMS LAMAT fields of temperature and geopotential height has been discussed briefly in Grose (1984). Winds derived from those fields have also been compared with rocket wind data for consistency by Smith and Bailey (1985), who found that, in general, the agreement is excellent. The LAMAT temperature data were not smoothed with latitude before generation of the LAMAT geopotential height fields. However, in the calculation of derived dynamical quantities, Grose (1984) applied an effective latitudinal smoother to the LAMAT temperatures using spherical harmonics (to give thickness fields for calculating winds and potential vorticity), while Smith and Bailey (1985) smoothed the geopotential height

prior to their wind calculations. Whatever the preference, one can work with either the LAMAT temperature or geopotential height fields.

In a separate effort, an intercomparison of the temperature, thickness, and various derived quantities was conducted for a small number of selected days using LIMS, SAMS, SSU, Free University of Berlin, and NMC analyses. The results of this intercomparison are available in MAP Handbook, Vol. 12 (Rodgers 1984), and the reader is referred to that study for further details. To illustrate the differences, a comparison of thickness maps (50–10 mbar) derived from LIMS is made in figure 18 with corresponding maps from the Berlin radiosonde analysis for January 2 and February 26.

For January 2 the general agreement is quite good. A noticeable difference however, is the “pinching” of the 10.4-km contour toward Russia ($\approx 60^\circ\text{N}$, 110°E) that is present in the Berlin map, but not in the LIMS map. Interestingly, the NMC map for January 2 shows this same effect, while a map based on the SAMS data agrees with the LIMS map and does not show this feature (Rodgers 1984). The maximum difference between the LIMS and Berlin thicknesses of approximately 500 meters (a difference of less than 5 percent) occurs at 50°N , 110°E near the “pinched” region. The reason for this difference is not known.

On February 26 the agreement between LIMS and Berlin again is quite good. The Berlin map displays a more pronounced trough extending (10°E , 50°N) than is evident in the LIMS map. Generally the difference in thicknesses between LIMS and Berlin is less than a few percent except in an extremely limited region near 80°N , 50°E , where differences are approximately 10 percent.

For regions above 10 mbar, satellite comparisons of thicknesses agree qualitatively well, but differ in details and magnitudes of gradients. The implied suggestion is that derived quantities (e.g., winds, heat and momentum flux, potential vorticity) may exhibit rather more significant differences than are apparent by examining and comparing height fields from different data sources.

Recall that the height fields were calculated from the temperatures with six zonal wave components assumed in the field. In those cases where some of these components were not calculated, zeros were used in the calculation. This occurred only at the 100-, 70-, and 0.05-mbar levels. The user may wish to go back to the temperature fields at these levels to see where this situation occurs; an example of the LAMAT (node 3) wave 2 and wave 5 temperature components is shown in figure 19 for the 100- and 50-mbar levels on January 7. The latitudinal variation in the 100-mbar wave 5 amplitude clearly

exhibits a sudden decrease from about 2 K at 28°S to zero at 24°S and extending to 20°N . The planetary-scale wave 2 amplitude profile, in contrast, is less affected by the cloud and noise contamination with zero values indicated for only the 12°S to 8°N region. The user should therefore bear these discontinuities, which may appear in the zonal mean, in mind when interpreting dynamical quantities related to the temperature and height fields in the subtropical lower stratosphere (e.g., static stability, eddy fluxes, potential vorticity). Since the 50-mbar level is used as the reference level for the LAMAT height fields, the lack of data at the 100- and 70-mbar levels does not affect the results from 50 to 0.05 mbar. Note that this would not be the case, however, should the user incorporate an alternative set of height data at the 100-mbar level (see below).

It is worth noting that the above discussion concerning the comparative usefulness of the LAMAT height fields is based on Northern, but not Southern, Hemisphere evaluations. Observational studies of the potential vorticity distribution on isentropic surfaces have been made for the Southern Hemisphere summertime zonal wave 5 phenomena utilizing the LAMAT height and temperature fields for January–February 1979. The level of spatial and temporal noise present in these daily potential vorticity analyses has made difficult a dynamically meaningful interpretation of the actual (eastward propagating) wave 5 vorticity signature. Subsequent investigations of the LAMAT and NMC NOPS data have shown that the relatively poor quality of the derived vorticity fields may be traced to analysis errors in the NMC 50-mbar NOPS height products, which in turn have arisen from hydrostatic contamination via asynoptic data assimilation problems during the tropospheric NMC operational (sea-level pressure to 100 mbar) Southern Hemisphere FGGE height analysis. Because of the relatively sparse distribution of radiosonde reports in southern middle and temperate latitudes, it is expected that any type of Southern Hemisphere synoptic height analysis will suffer from these problems in a more acute fashion than would an analysis for the Northern Hemisphere. Potential users of the LAMAT Southern Hemisphere heights should therefore be aware of the NMC base level difficulties and, furthermore, may find it quite fruitful to generate an additional LIMS height data base from a combination of the LAMAT temperature (thickness) data and an alternative base level data source, such as that produced by the Free University of Berlin.

Concluding Remarks

A rather simple Kalman filter is described in this paper for analyzing asynoptic data from LIMS. This

application uses a Fourier series, in which not more than 13 coefficients, that is, 6 wave components, are calculated, thereby producing maps which are the best estimates of the synoptic fields at noon GMT. These coefficients comprise the data on the LIMS Map Archival Tape (LAMAT).

The following judgments were derived from the operational LAMAT development. The calculation of parts of the virtual data set from the results of a series of preliminary filter runs works well, and the diagnostics used in conjunction with the filter provide sensitive detection of interesting and unexpected results, as well as location of occasional bad data. The filter follows time variations quite well, but this is due in part to the excellent quality of the LAIPAT data.

In retrospect, several changes to the LAMAT processing procedure were evaluated. First, the LAIPAT data, which were within 1° of the desired latitudes, could have, in most cases, been interpolated to the exact latitude at which the Kalman filtering was done. This represents only a minor improvement. Second, when there was a significant diurnal variation, the results for the combined node could have been improved by altering the procedure for constructing the combined data set. Instead of using all the data as it is on the LAIPAT for this set, it could be constructed from the ascending and descending node sets as follows. First, calculate the mean value of the ascending node for the time period desired; represent this by $T_{A,avg}$. Then subtract this average from each ascending node data point. Repeat this procedure for the descending node set. Let the two sets after the removal of the averages be T_A and T_D . The combined node can now be constructed as

the sum of T_A , T_D , and the average of T_A and T_D , or

$$T_C = T_A + T_D + \frac{T_{A,avg} + T_{D,avg}}{2}$$

This procedure for constructing the combined node (T_C) removes the mean diurnal variation from the data set. Of course if there is a time-dependent term in the diurnal variation it is still present. This procedure has two advantages. First, it removes the dependence of the zonal mean term on the relative number of ascending and descending data points. Second, the absence of the diurnal variation will improve the calculation of the slower wave components in the field. Since the filter cannot resolve the diurnal components, it is best to remove these components before applying the filter.

There is a certain degree of time smoothing done by the Kalman filter, but this has been kept to a minimum consistent with the nature of the observed fields. However, some features have been eliminated or smoothed out by the processing. These include diurnal waves (for the combined node), fast traveling waves, and very transient features. The degree of smoothing in each of these cases depends on both the filter input parameters and the time density of measured data input. To determine effects of such smoothing, it is always possible to examine the LAIPAT data and compare them with the predictions of the LAMAT, as was done in this report.

NASA Langley Research Center
Hampton, VA 23665-5225
January 31, 1986

Appendix

The LAMAT Format

The basic format for the LAMAT is given in the NOPS requirements document #NG-52, Rev. B (1980), which is available from NSSDC. The archived LAMAT contains several modifications, as noted below.

The spectral coefficients for each day and latitude have been used to calculate a standard deviation (σ_{obs}) for each day and latitude. The σ_{obs} value was calculated from the differences between the LIMS asynoptic LAIPAT orbital data and the estimate obtained using the spectral coefficients at the same longitude for that day and latitude. No time interpolation was applied to the coefficients, and the σ_{obs} includes the effects of time variations as well as differences due to the usual curve-fitting errors. If there were not enough data to calculate a standard deviation, the value was set to -1 . This information should help in judging the suitability of the coefficients for a particular study.

The standard deviations have been written into words 2 through 115 of the LAMAT record. The tangent point latitude-longitude pairs have not been written to this record. The standard deviations are packed into 24-bit words. The first block of 38 values, 64°S to 84°N , are for the ascending node and are in words 2 through 39. Words 40 through 77 are the descending node values, and words 78 through 115 are the combined node values. These values should be unpacked in the same way as the coefficients for the same node. That is, the same offset (10^5) and the same scale factor apply. The remaining 12864 bits of this data block are unused in the LAMAT.

The node flags show the maximum number of waves that may be present in any one latitude for this parameter (i.e., temperature, geopotential height, or trace gas species), day, pressure level, and node. The flags do not indicate that all these waves are present for all latitudes. When the average number of data points per day, during a Kalman filter processing run, became too small to justify the calculation of the desired number of waves, the number of waves was reduced. The coefficients that were not calculated were, of course, set to zero. That is, the coefficient is zero after the packing and scaling have been done. (Because of the scale factor of 1000 used for all coefficients and the offset of (10^5), these uncalculated coefficients are unpacked as -100 . On rare occasions a coefficient may be unpacked as 0.0 if it was calculated and subsequently truncated to zero during the packing process.) If both the sine and the cosine coefficient is zero for any wave and all shorter waves, then no data were analyzed at that wave number.

The algorithm identifier was set to 2. The units code is as follows

5	ppmv
6	ppbv
17	kilometers
18	Kelvin

Codes for time coverage are

1	daily maps centered on synoptic time
2	monthly mean maps
3	seasonal mean maps

The beginning orbit number, ending orbit number, and number of inclusive orbits are zero filled.

TABLE 1. LIMS ACCURACY, PRECISION, AND CORRELATIVE COMPARISON RESULTS

Parameter	Estimated ^a accuracy	Correlative comparison	Estimated precision
Temperature	^b < 2 K	< 2 K	< 0.2 K–0.6 K
Ozone mixing ratio	16–41%	< 10%	< 0.25 ppmv
Water vapor mixing ratio	18–36%	< 20%	< 0.25 ppmv
Nitric acid mixing ratio	17–45%	20–50%	< 0.15 ppbv
Nitrogen dioxide mixing ratio	20–50%	< 20%	< 0.25 ppbv

^aRange is variation over altitude.^bFor pressure > 1 mbar.

TABLE 2. DATA VARIANCE FOR JANUARY 13 TO
FEBRUARY 12, 1979

Pressure, mbar	Temperature variance, K ²	Latitudes, deg
70.0	0.45	64.0S to Equator
	.75	4.0N to 32.0N
	.35	16.0N to 56.0N
	.6	60.0N to 83.5N
30.0	.25	64.0S to 24.0N
	.6	28.0N to 44.0N
	.3	48.0N to 83.5N
10.0	1.0	64.0S to 40.0S
	.4	36.0S to 32.0N
	.8	36.0N to 68.0N
	.4	72.0N to 83.5N
5.0	.8	64.0S to 52.0N
	.6	48.0N to 83.5N
2.0	1.2	64.0S to 52.0S
	.5	48.0S to Equator
	1.2	4.0N to 12.0N
	.8	16.0N to 83.5N
1.0	1.2	64.0S to 52.0S
	.6	48.0S to Equator
	1.5	4.0N to 12.0N
	1.0	16.0N to 83.5N
.5	1.2	64.0S to 52.0S
	.8	48.0S to Equator
	1.8	4.0N to 12.0N
	1.0	16.0N to 83.5N
.2	1.2	64.0S to 52.0S
	.5	48.0S to 20.0S
	1.0	16.0S to Equator
	1.5	4.0N to 12.0N
	1.0	16.0N to 56.0N
	2.0	60.0N to 68.0N
	1.0	72.0N to 83.5N

TABLE 3. RELAXATION TIMES FOR JANUARY 12 TO FEBRUARY 12, 1979

Pressure, mbar	Relaxation time, days, for wave number—						
	0	1	2	3	4	5	6
70.0	5.11	5.77	4.76	3.74	2.52	2.60	2.69
30.0	5.29	4.30	4.30	4.30	2.50	2.50	2.50
10.0	3.34	4.20	4.20	3.10	3.10	2.50	2.50
5.0	3.69	3.80	3.80	3.80	2.00	2.00	1.55
2.0	3.44	3.78	2.66	2.20	1.50	1.50	1.50
1.0	4.11	3.30	3.00	3.00	2.29	2.00	2.00
.5	4.15	3.70	2.70	2.24	2.00	2.00	2.00
.2	4.35	3.50	3.00	2.00	2.00	2.00	2.00

TABLE 4. DAYS WITH INTERPOLATED 50-mbar REFERENCE HEIGHT DATA

Month	Northern Hemisphere	Southern Hemisphere
Oct. 1978		25, 30
Nov.	7, 17, 27	1, 2, 13, 16
Dec.		19
Jan. 1979		4, 21, 24, 25
Feb.		23
Mar.		4, 5, 7, 17
Apr.		12
May	13, 23	7, 11

References

- Gille, J. C.; Bailey, P. L.; and Russell, J. M., III 1980: Temperature and Composition Measurements From the L.R.I.R. and L.I.M.S. Experiments on Nimbus 6 and 7. *Philos. Trans. R. Soc. London*, ser. A, vol. 296, no. 1418, Mar. 6, pp. 205-218.
- Gille, John C.; and Russell, James M., III 1984: The Limb Infrared Monitor of the Stratosphere: Experiment Description, Performance and Results. *J. Geophys. Res.*, vol. 89, no. D4, June 30, pp. 5125-5140.
- Gille, John C.; Russell, James M., III; Bailey, Paul L.; Gordley, Larry L.; Remsberg, Ellis E.; Lienesch, James H.; Planet, Walter G.; House, Frederick B.; Lyjak, Lawrence V.; and Beck, Sharon A. 1984a: Validation of Temperature Retrievals Obtained by the Limb Infrared Monitor of the Stratosphere (LIMS) Experiment on Nimbus 7. *J. Geophys. Res.*, vol. 89, no. D4, June 30, pp. 5147-5160.
- Gille, John C.; Russell, James M., III; Bailey, Paul L.; Remsberg, Ellis E.; Gordley, Larry L.; Evans, Wayne F. J.; Fischer, Herbert; Gandrud, Bruce W.; Girard, Andre; Harries, John E.; and Beck, Sharon A. 1984b: Accuracy and Precision of the Nitric Acid Concentrations Determined by the Limb Infrared Monitor of the Stratosphere Experiment on NIMBUS 7. *J. Geophys. Res.*, vol. 89, no. D4, June 30, pp. 5179-5190.
- Greville, T. N. E. 1967: Spline Functions, Interpolation, and Numerical Quadrature. *Mathematical Methods for Digital Computers, Volume II*, Anthony Ralston and Herbert S. Wilf, eds., John Wiley & Sons, Inc., pp. 156-168.
- Grose, William L. 1984: Recent Advances in Understanding Stratospheric Dynamics and Transport Processes: Application of Satellite Data to their Interpretation. *Adv. Space Res.*, vol. 4, no. 4, pp. 19-28.
- Hitchman, Matthew H.; and Leovy, Conway B. 1985: Diurnal Tide in the Equatorial Middle Atmosphere as Seen in LIMS Temperatures. *J. Atmos. Sci.*, vol. 42, no. 6, Mar. 15, pp. 557-561.
- Kohri, William James 1981: *LRIR Observations of the Structure and Propagation of the Stationary Planetary Waves in the Northern Hemisphere During December 1975*. NCAR/CT-63 (Contract ATM 77-23757), Nat. Center Atmos. Res. (Available from NTIS as PB82 156 639.)
- McCormick, M. P.; Steele, H. M.; Hamill, Patrick; Chu, W. P.; and Swissler, T. J. 1982: Polar Stratospheric Cloud Sightings by SAM II. *J. Atmos. Sci.*, vol. 39, no. 6, June, pp. 1387-1397.
- Quiroz, Roderick S. 1979: Tropospheric-Stratospheric Interaction in the Major Warming Event of January-February 1979. *Geophys. Res. Lett.*, vol. 6, no. 8, Aug., pp. 645-648.
- Remsberg, Ellis E.; Russell, James M., III; Gille, John C.; Gordley, Larry L.; Bailey, Paul L.; Planet, Walter G.; and Harries, John E. 1984: The Validation of NIMBUS 7 LIMS Measurements of Ozone. *J. Geophys. Res.*, vol. 89, no. D4, June 30, pp. 5161-5178.
- Rodgers, C. D. 1976: Retrieval of Atmospheric Temperature and Composition From Remote Measurements of Thermal Radiation. *Rev. Geophys. & Space Phys.*, vol. 14, no. 4, Nov., pp. 609-624.
- Rodgers, C. D. 1977: Statistical Principles of Inversion Theory. *Inversion Methods in Atmospheric Remote Sounding*, Adarsh Deepak, ed., Academic Press, Inc., pp. 117-138.
- Rodgers, C. D., ed. 1984: *Middle Atmosphere Program—Handbook for MAP, Volume 12*. SCOSTEP Secretariat, Univ. of Illinois, July.
- Russell, J. M.; and Gille, J. C. 1978: The Limb Infrared Monitor of the Stratosphere (LIMS) Experiment. *The Nimbus 7 Users' Guide*, Charles R. Madrid, ed., NASA Goddard Space Flight Center, Aug., pp. 71-103. (Available as NASA TM-79969.)
- Russell, James M., III; Gille, John C.; Remsberg, Ellis E.; Gordley, Larry L.; Bailey, Paul L.; Drayson, S. Roland; Fischer, Herbert; Girard, Andre; Harries, John E.; and Evans, Wayne F. J. 1984a: Validation of Nitrogen Dioxide Results Measured by the Limb Infrared Monitor of the Stratosphere (LIMS) Experiment on Nimbus 7. *J. Geophys. Res.*, vol. 89, no. D4, June 30, pp. 5099-5107.
- Russell, James M.; Gille, John C.; Remsberg, Ellis E.; Gordley, Larry L.; Bailey, Paul L.; Fischer, Herbert; Girard, Andre; Drayson, S. Roland; Evans, Wayne F. J.; and Harries, John E. 1984b: Validation of Water Vapor Results Measured by the Limb Infrared Monitor of the Stratosphere Experiment on Nimbus 7. *J. Geophys. Res.*, vol. 89, no. D4, June 30, pp. 5115-5124.
- Smith, A. K.; and Bailey, P. L. 1985: Comparison of Horizontal Winds From the LIMS Satellite Instrument With Rocket Measurements. *J. Geophys. Res.*, vol. 90, no. D2, Apr. 20, pp. 3897-3901.

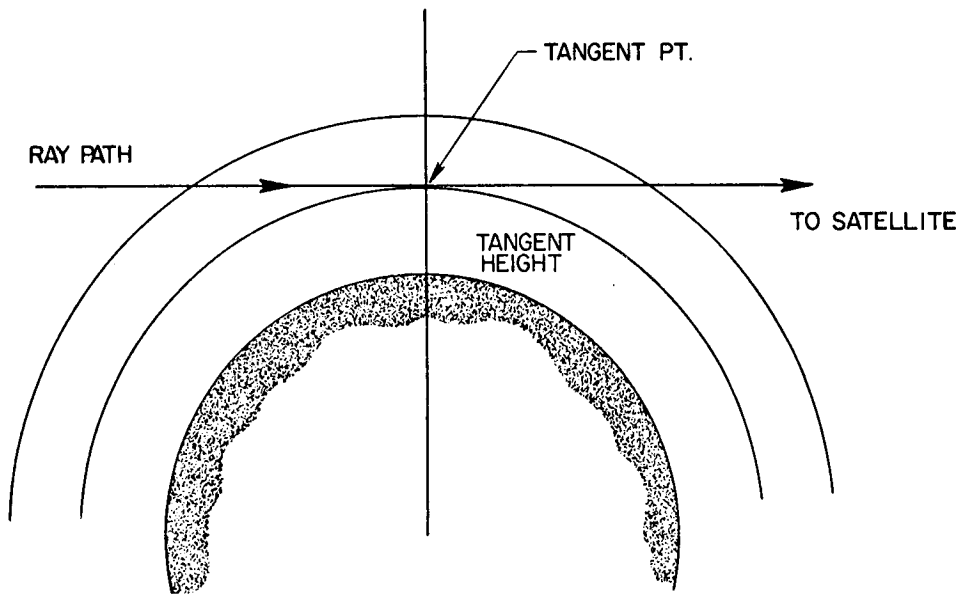


Figure 1. Tangent height and ray path.

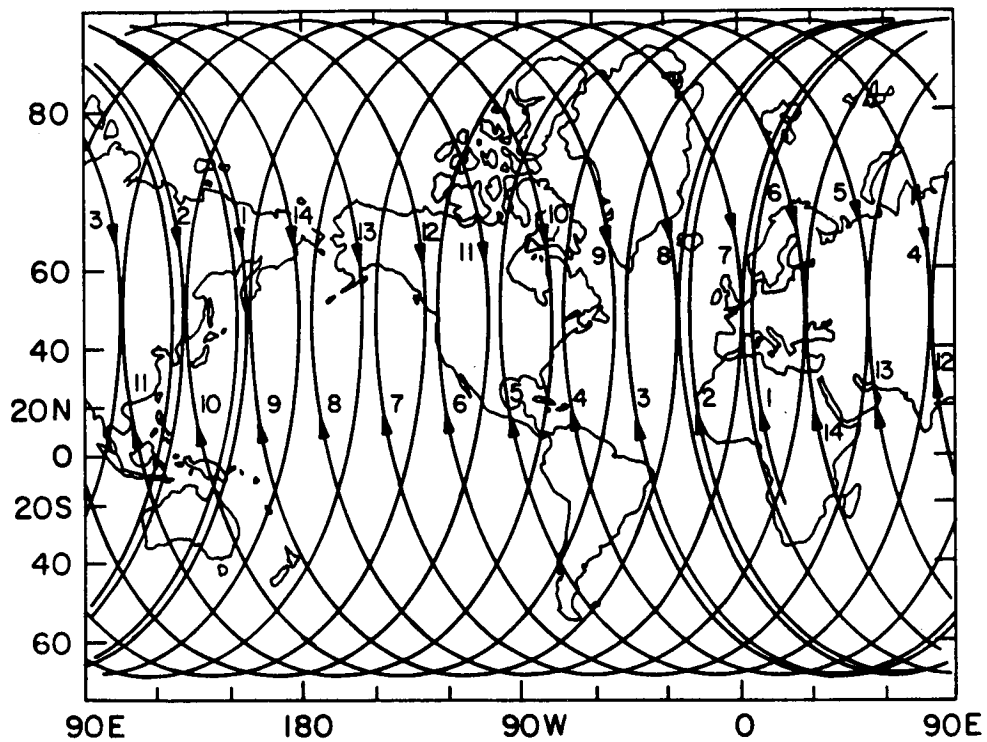


Figure 2. LIMS data coverage per day.

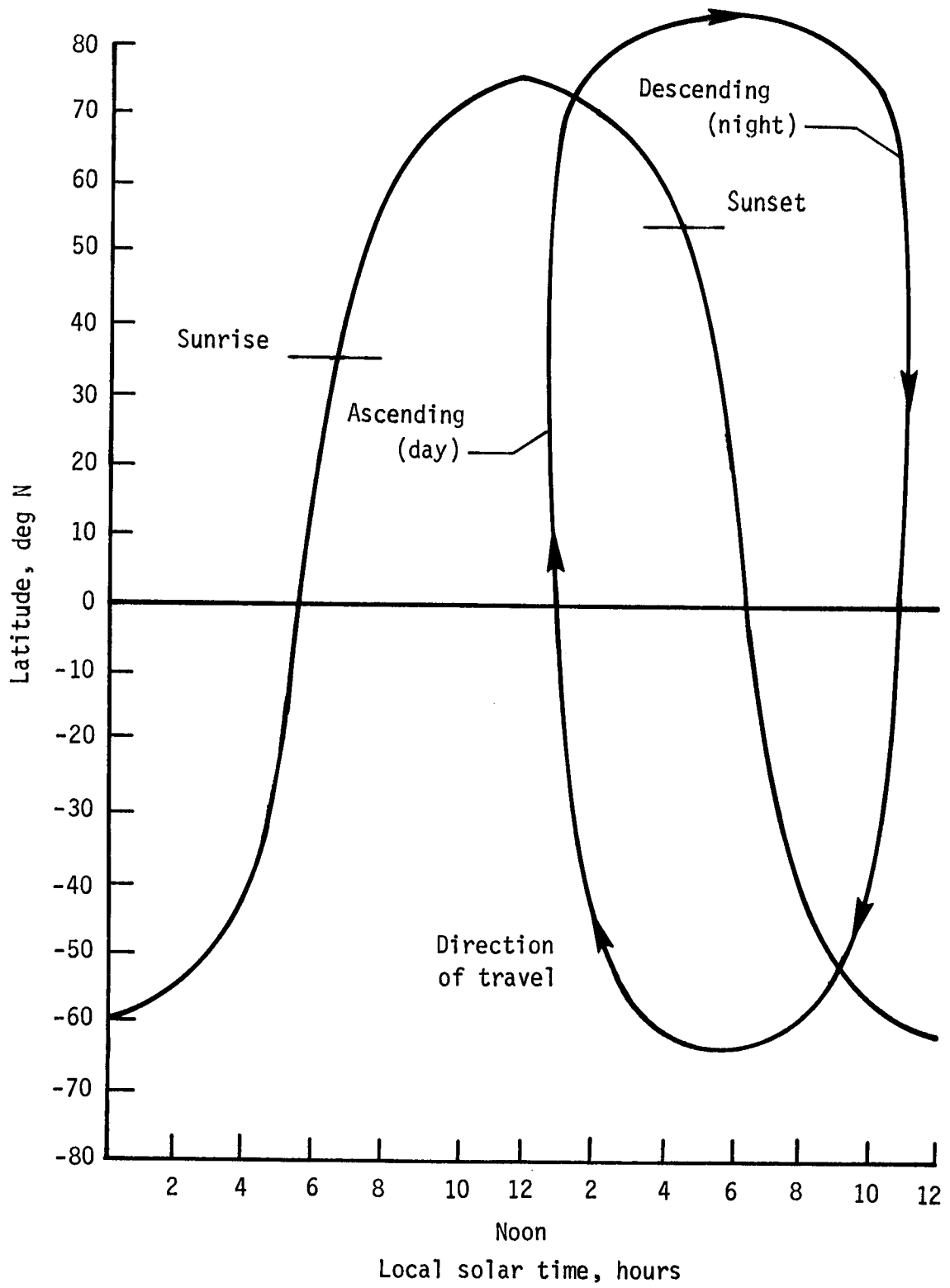


Figure 3. Tangent point track and 30 km terminator location on latitude vs. local solar time grid.

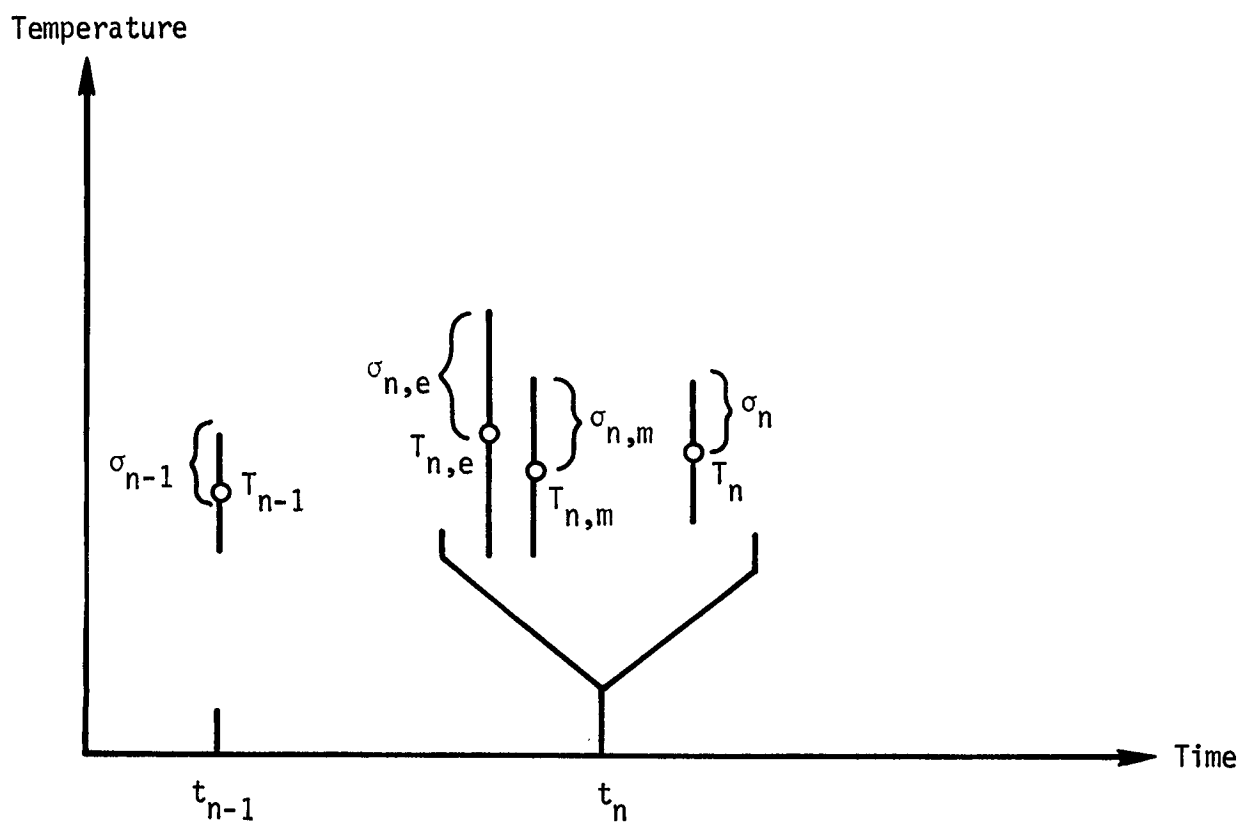
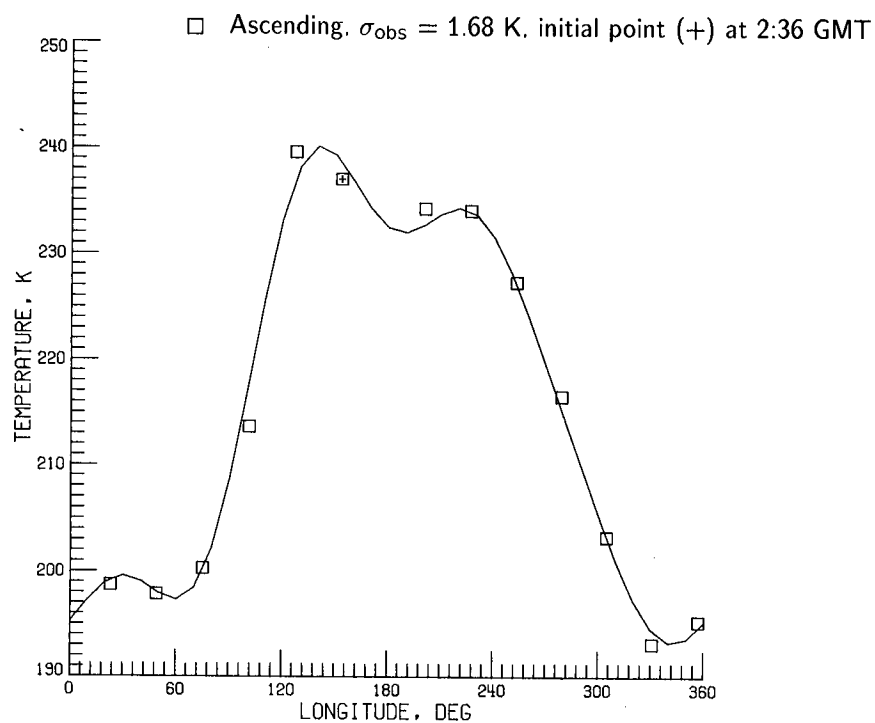
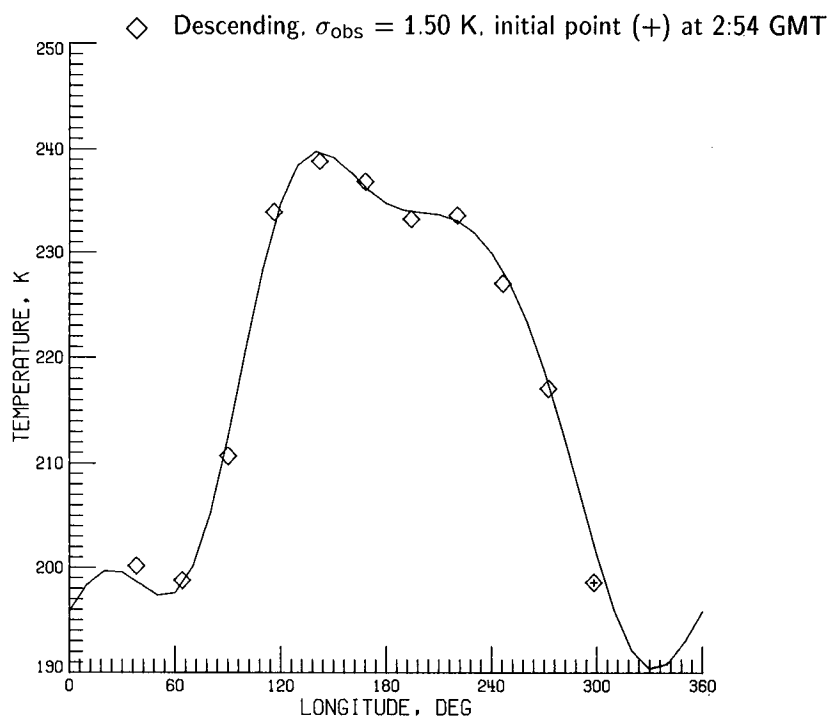


Figure 4. Schematic of time update for Kalman filter.

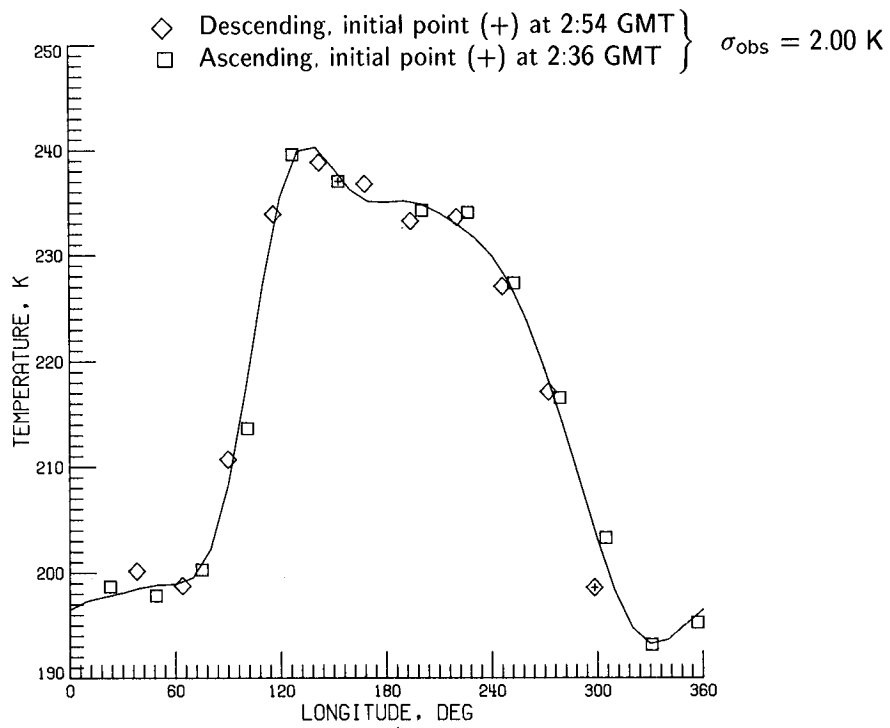


(a) Ascending node.



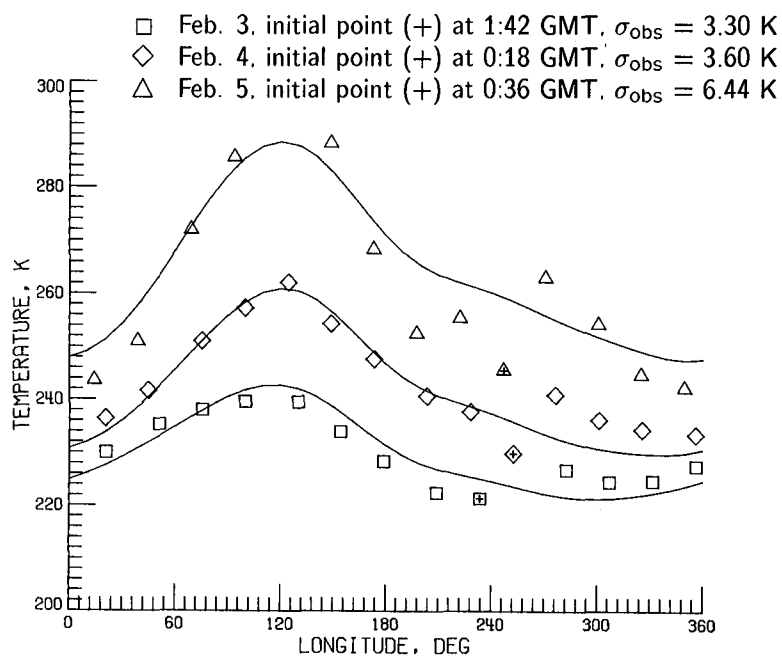
(b) Descending node.

Figure 5. Measured and LAMAT temperatures for 30 mbar, 60°N on Jan. 26, 1979.

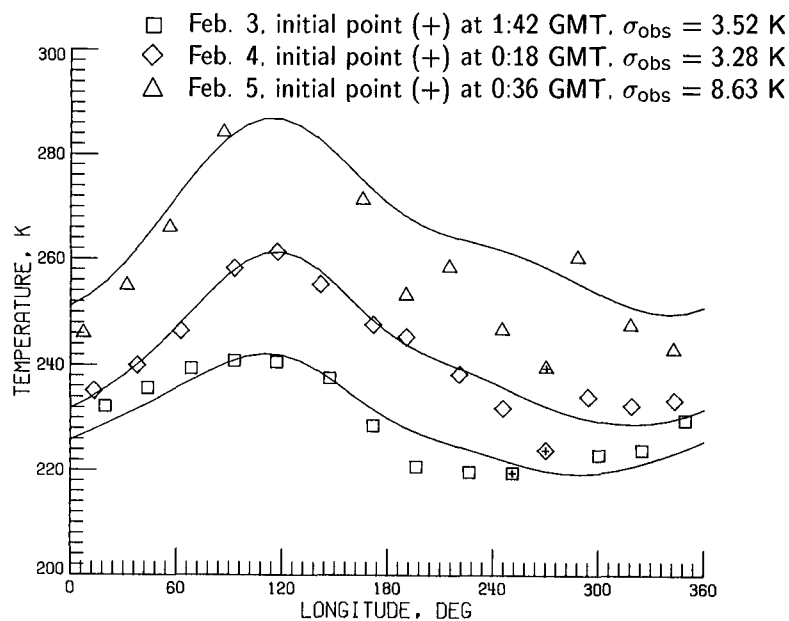


(c) Combined node.

Figure 5. Concluded.

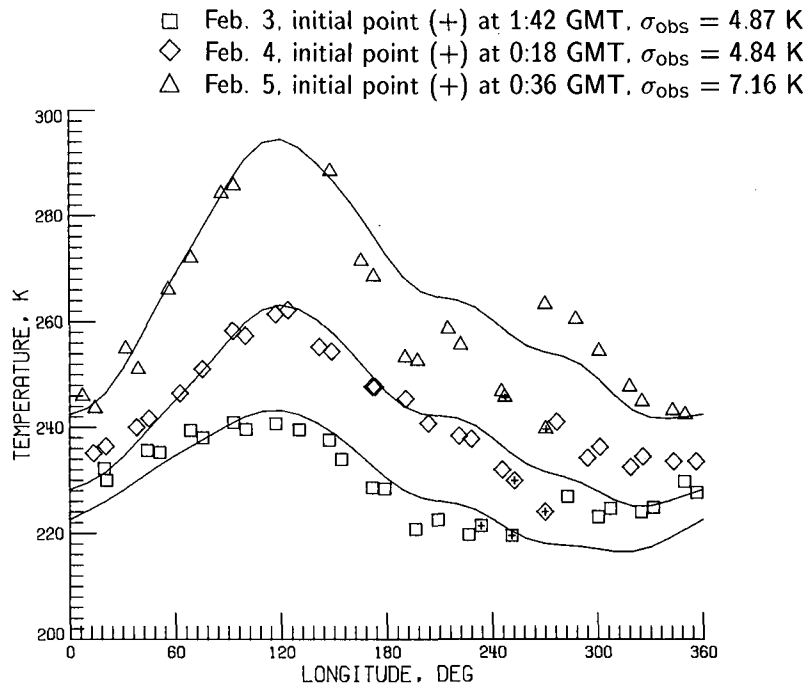


(a) Ascending node.



(b) Descending node.

Figure 6. Measured and LAMAT temperatures for 5 mbar, 83.5°N on Feb. 3–5, 1979.



(c) Combined node.

Figure 6. Concluded.

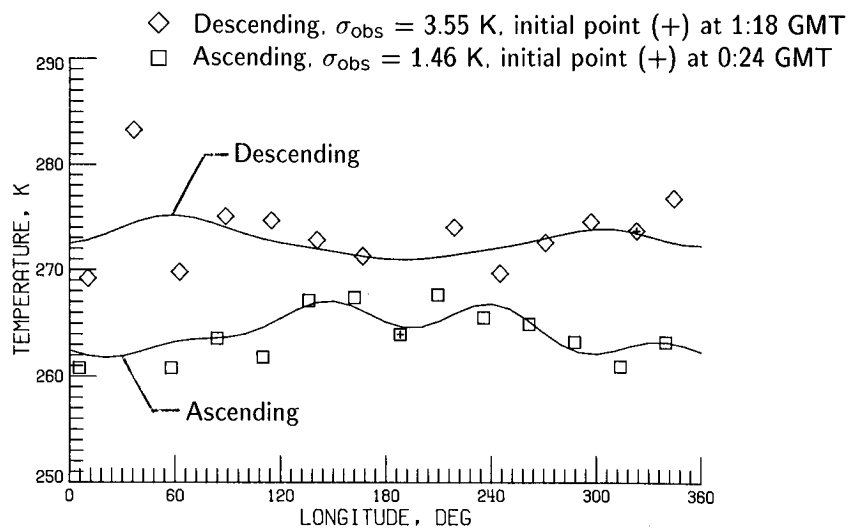
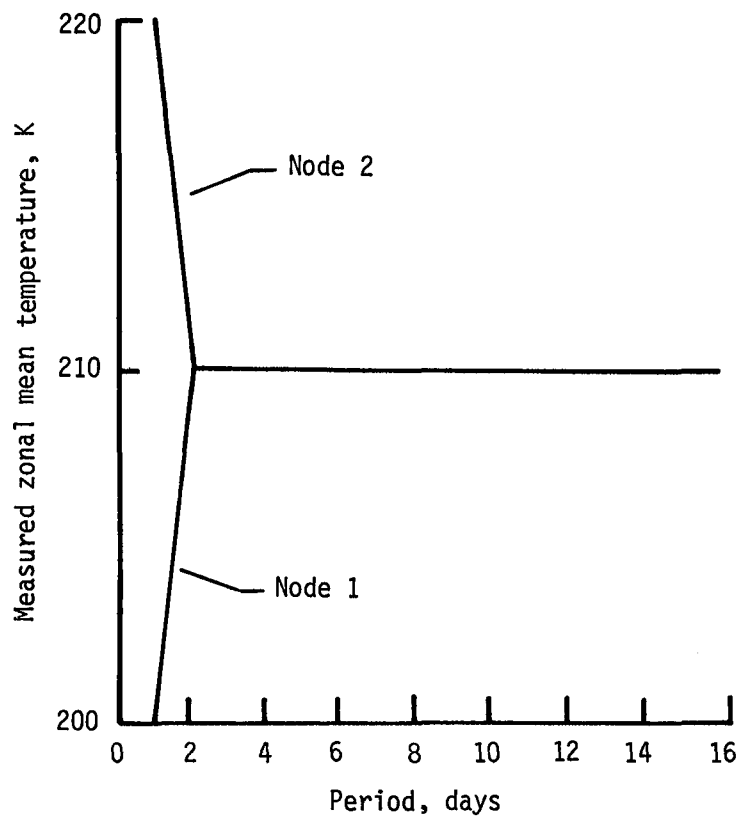
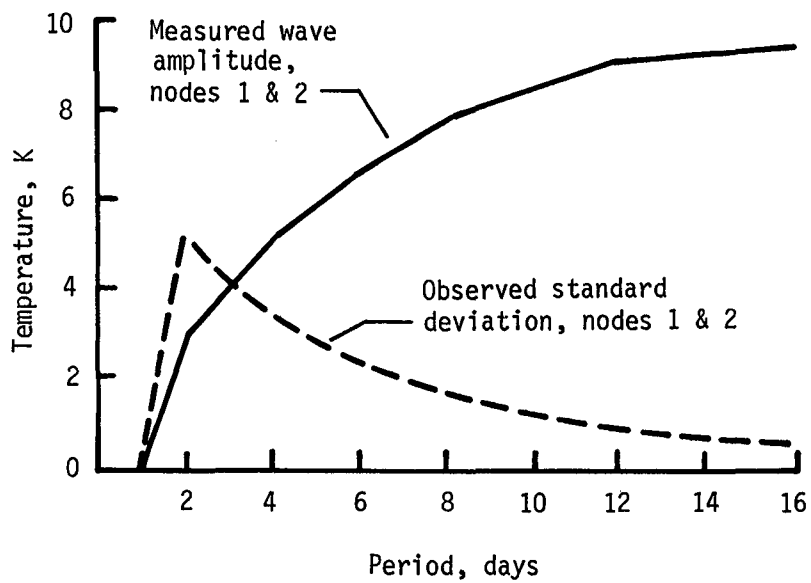


Figure 7. Measured and LAMAT temperatures for 0.7 mbar, 0°N on Feb. 23, 1979 (ascending and descending nodes).

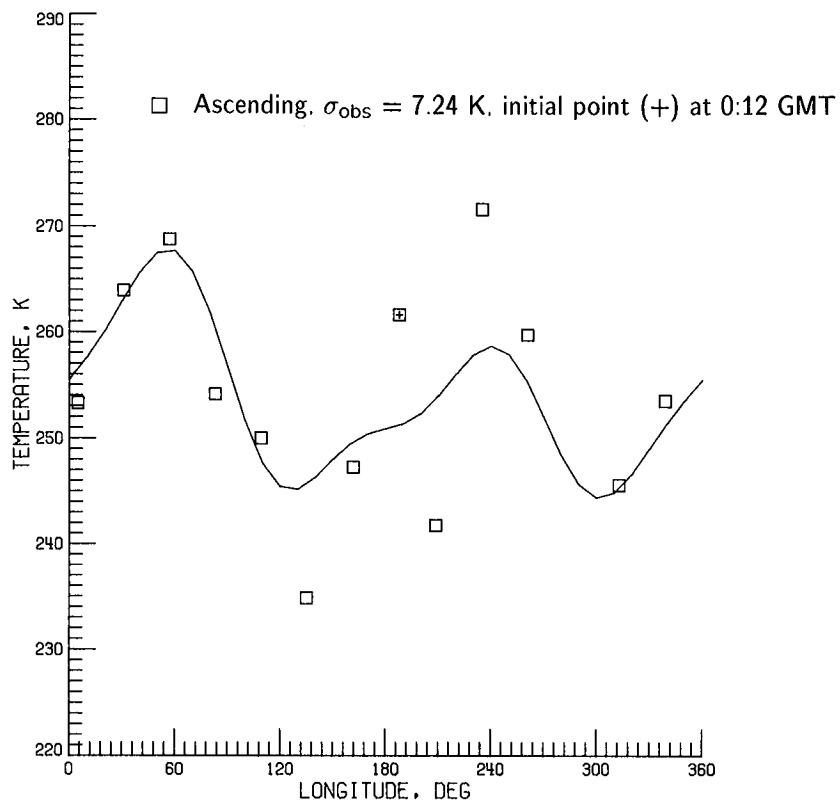


(a) Zonal mean for ascending and descending nodes.

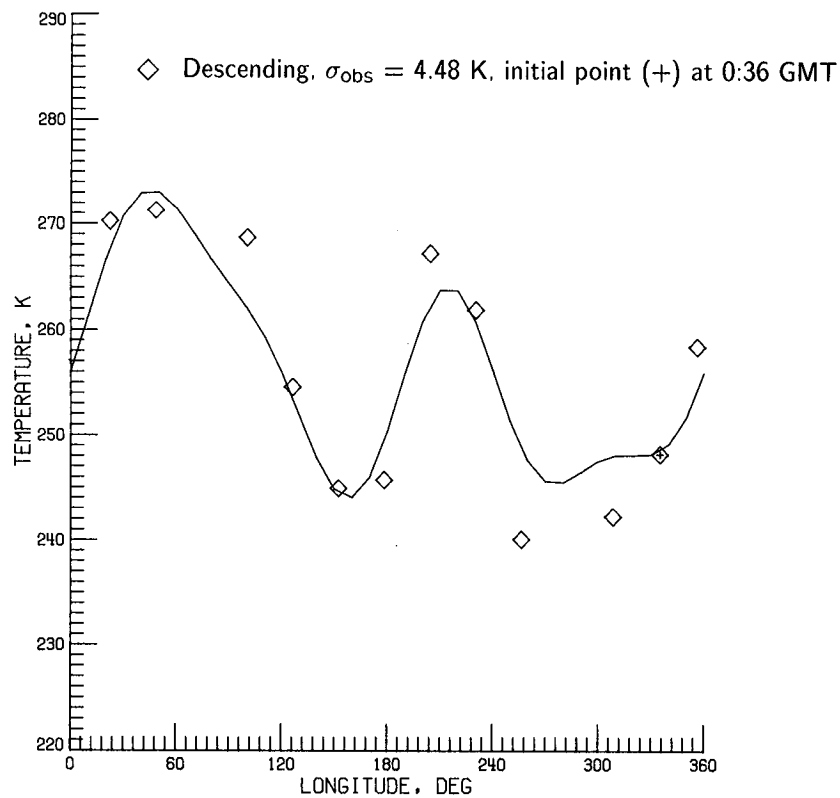


(b) Wave 1 amplitudes for ascending and descending nodes, and observed standard deviations.

Figure 8. Response of Kalman filter to a simulated traveling wave.

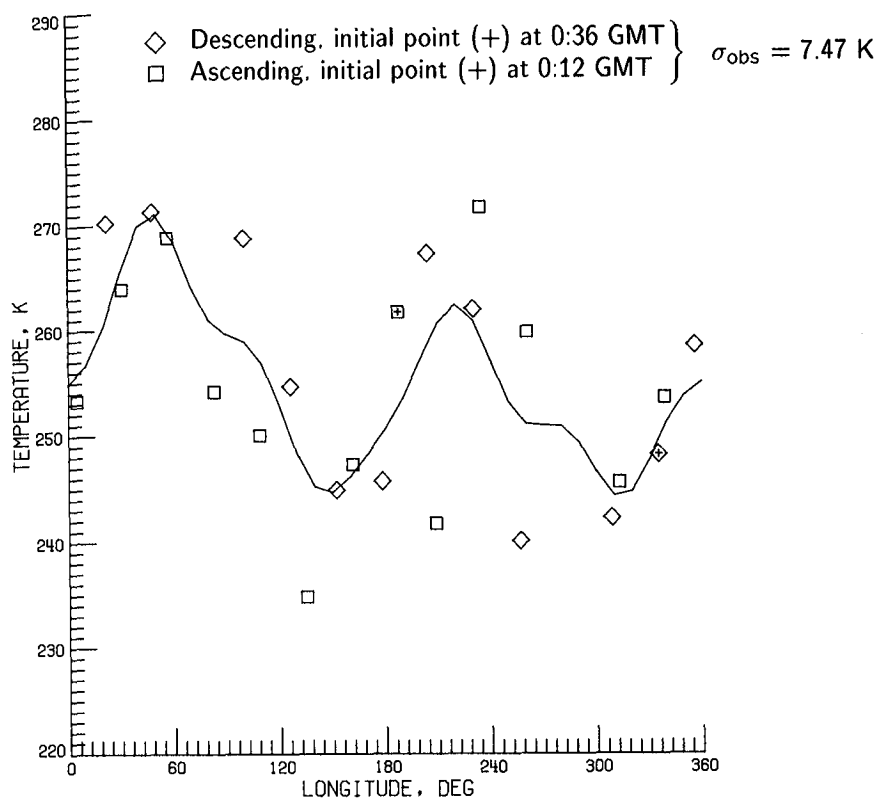


(a) Ascending node.



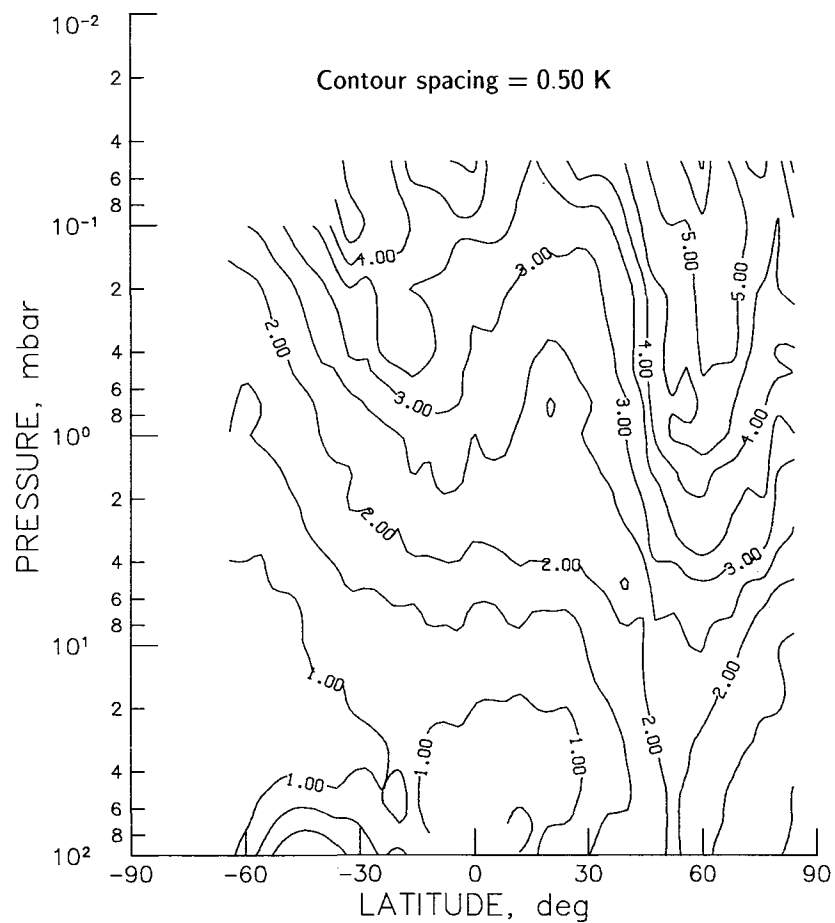
(b) Descending node.

Figure 9. Measured and LAMAT temperatures for 1 mbar, 52°N on Dec. 14, 1978.

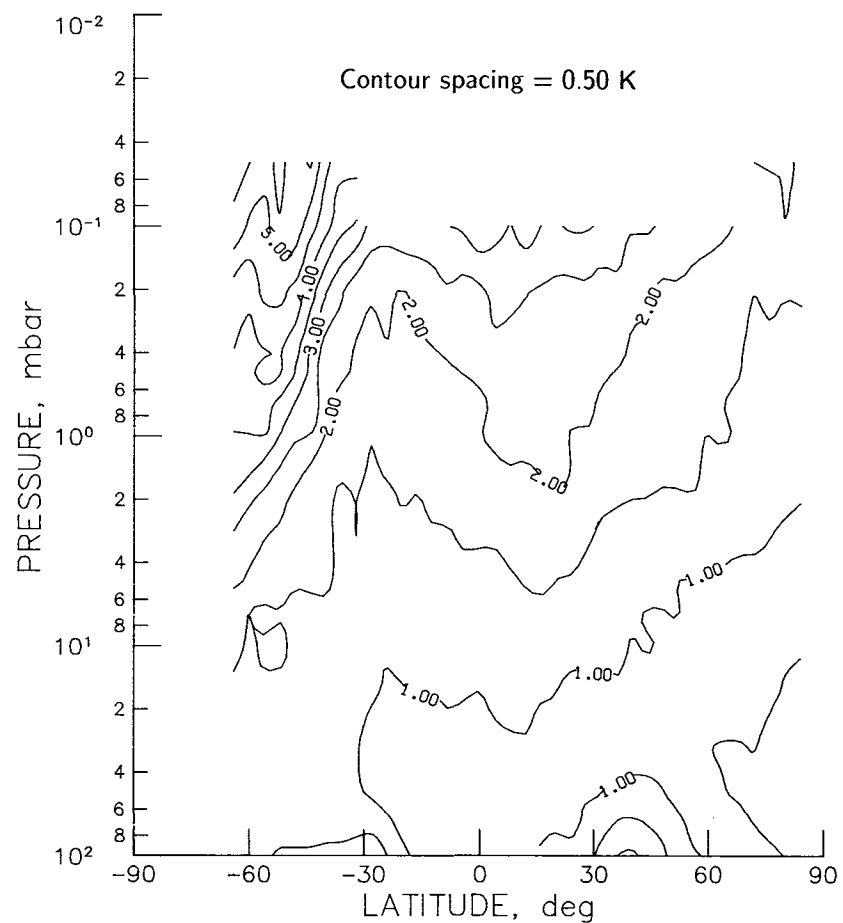


(c) Combined node.

Figure 9. Concluded.

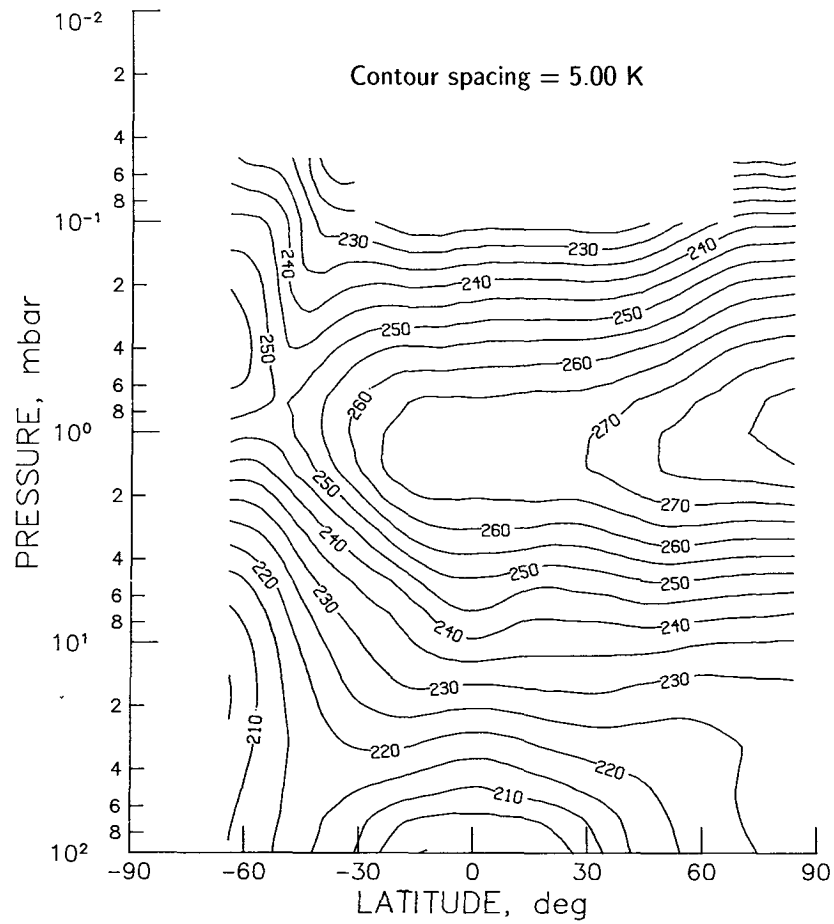


(a) January 1979.

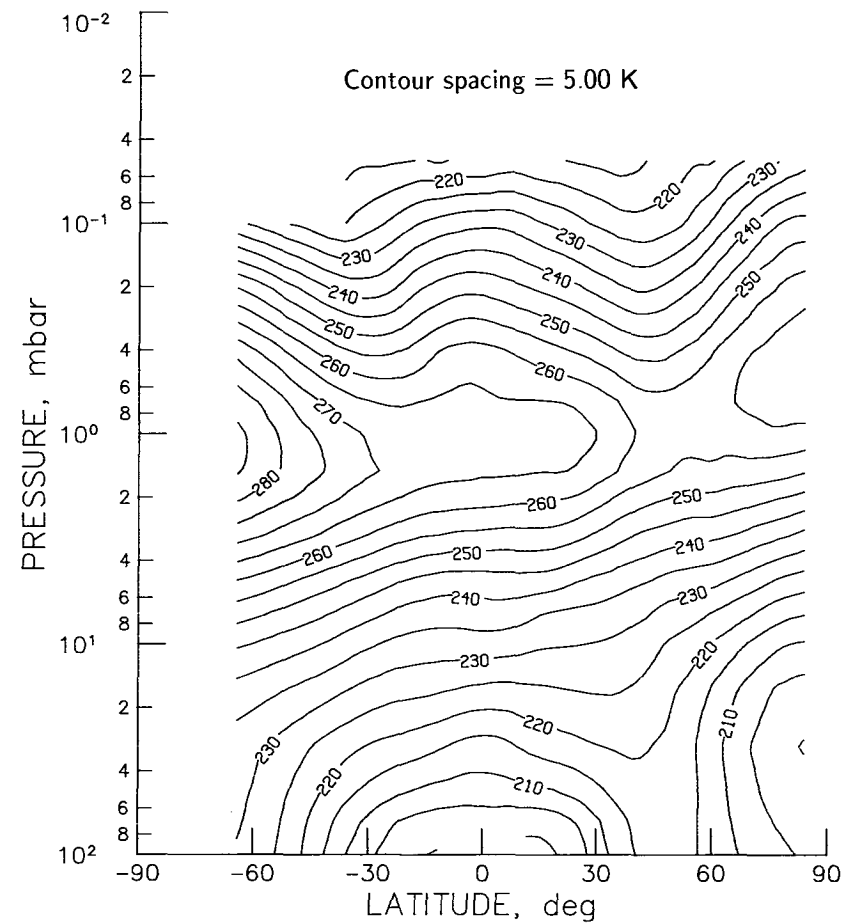


(b) May 1979.

Figure 10. Monthly mean values of standard deviations of ascending node LAMAT temperature from observations.

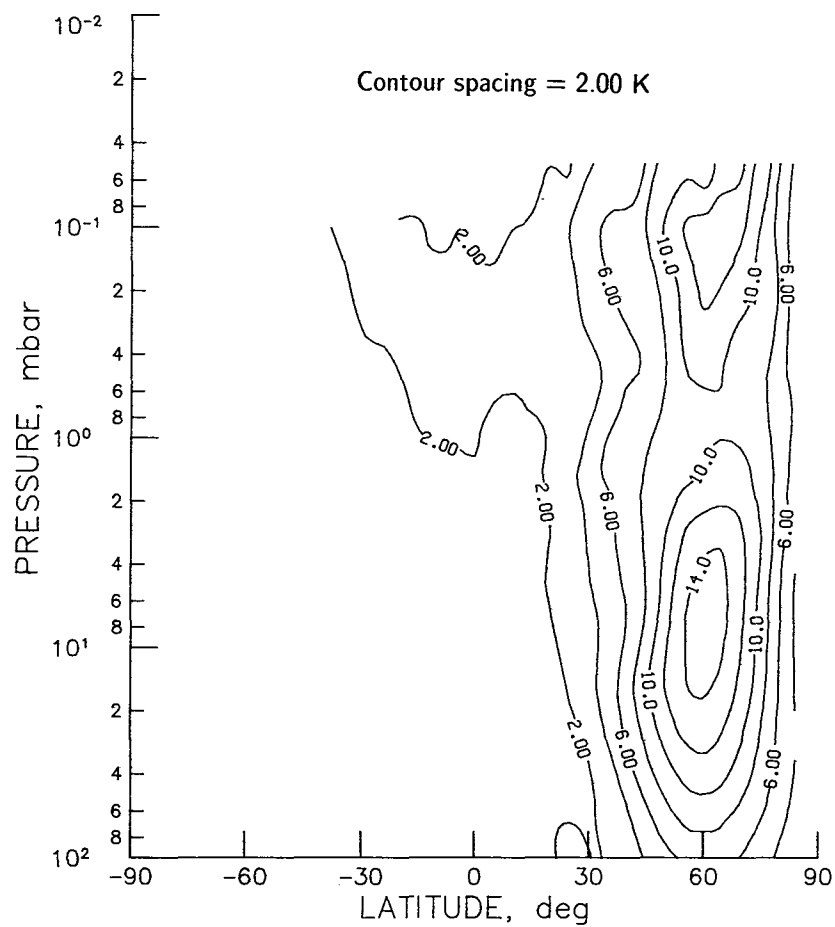


(a) January 1979.

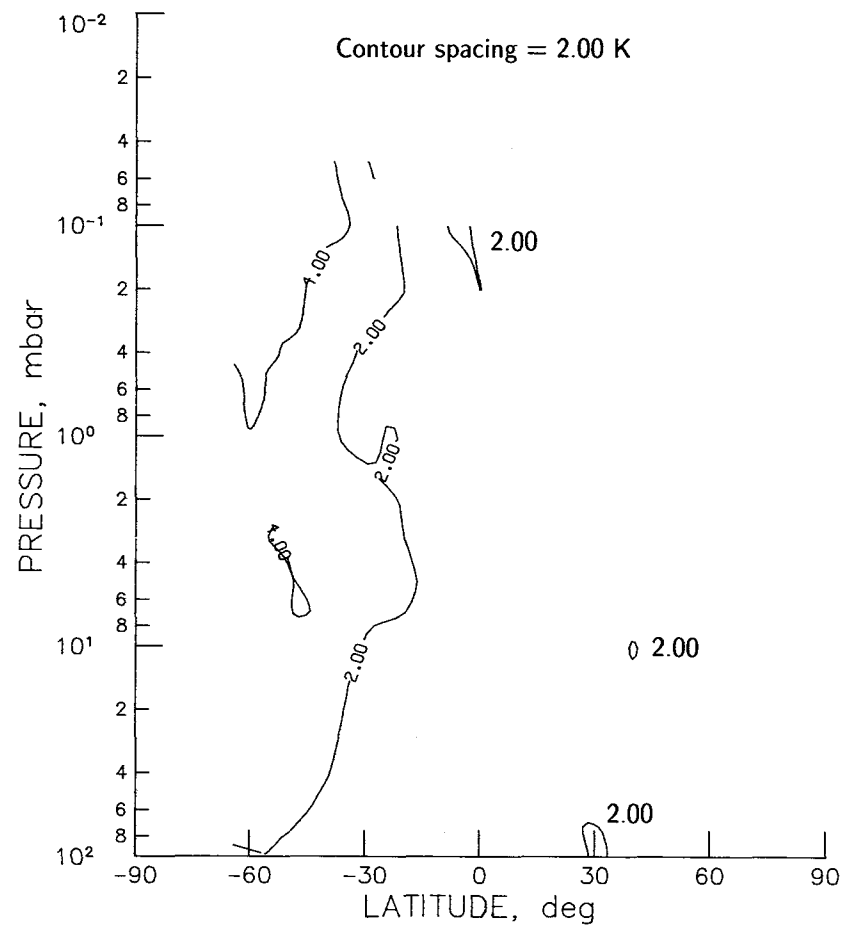


(b) May 1979.

Figure 11. Monthly mean of zonal mean ascending node LAMAT temperature.

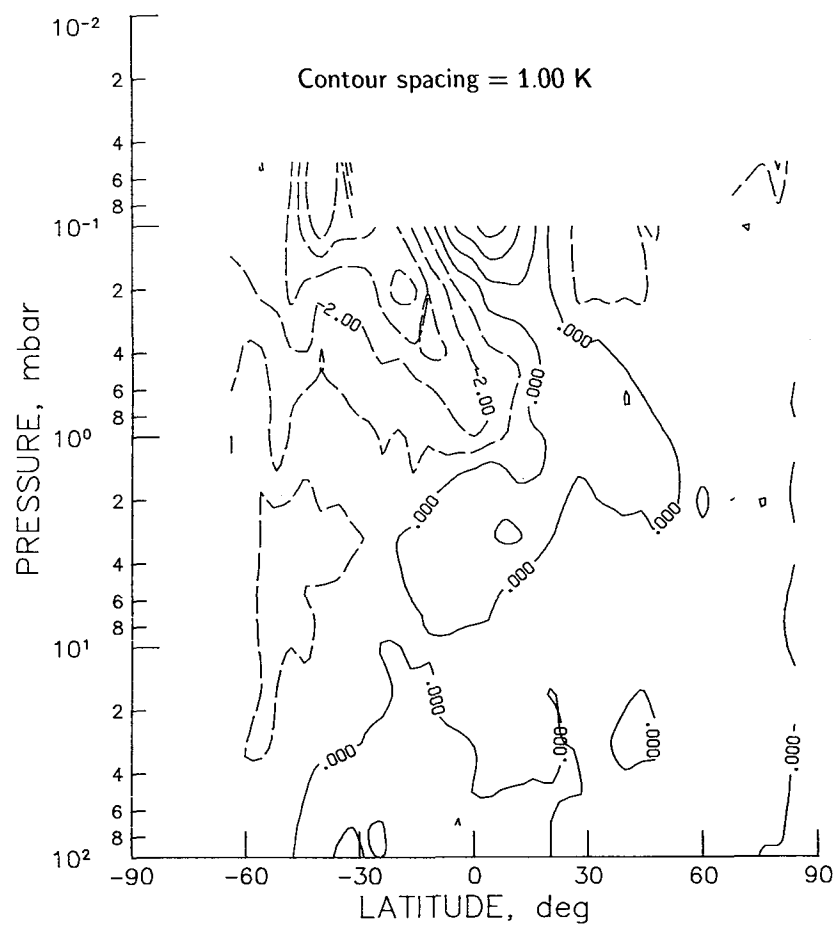


(a) January 1979.

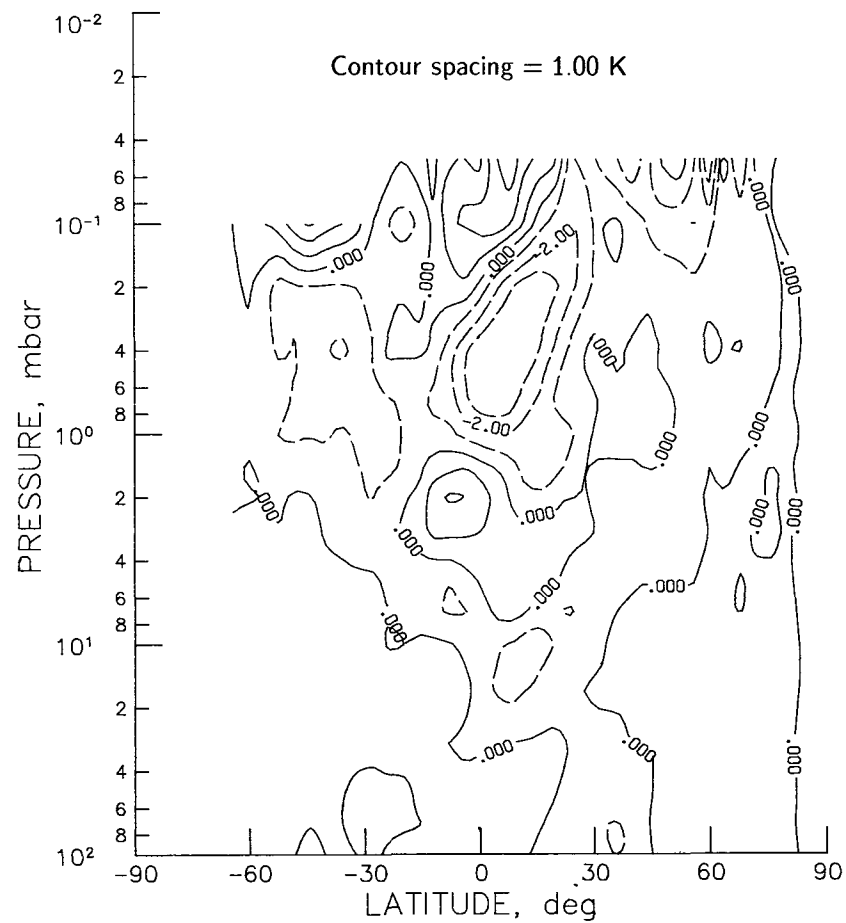


(b) May 1979.

Figure 12. Monthly mean standard deviations of the LAMAT temperature from their daily zonal means.

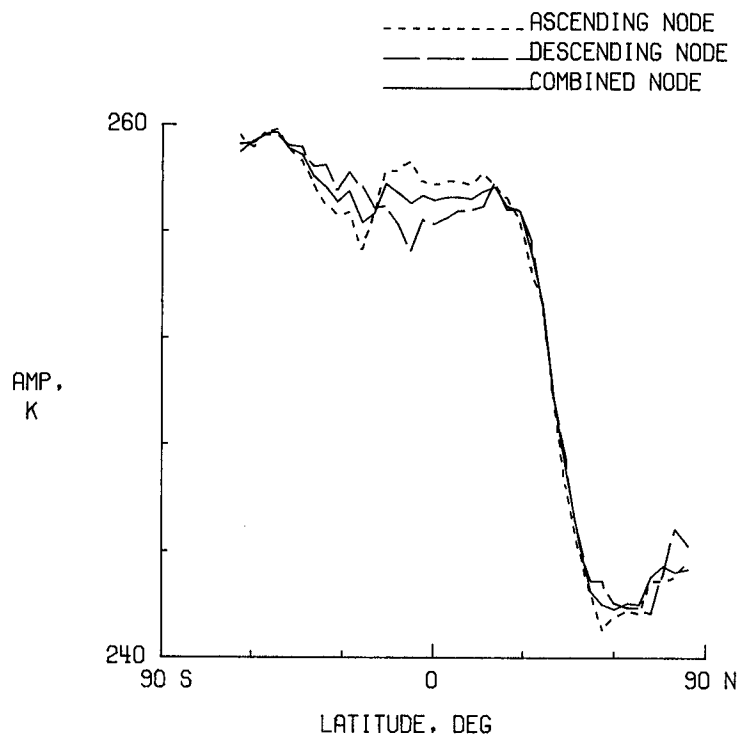


(a) January 1979.

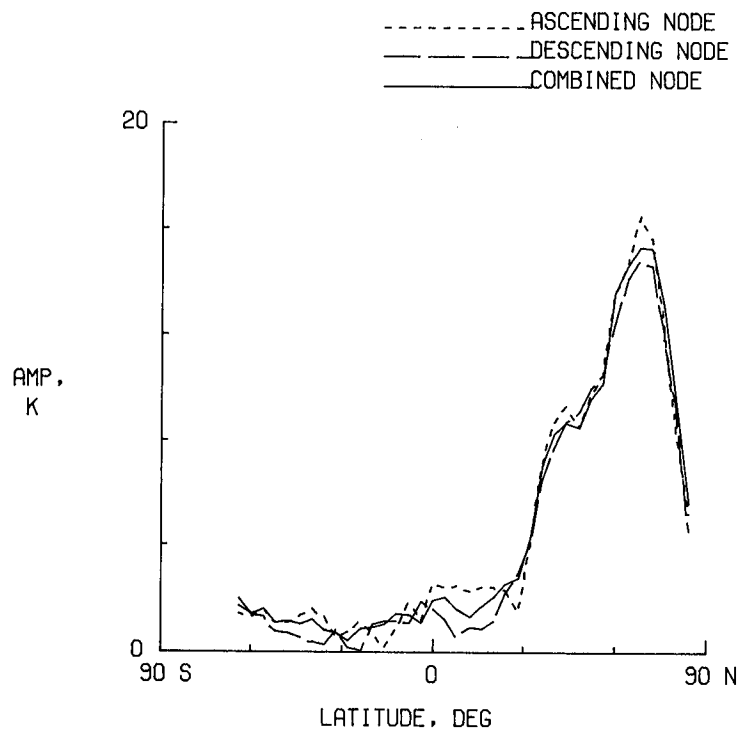


(b) May 1979.

Figure 13. Monthly mean differences between the ascending and descending node zonal mean LAMAT temperatures.

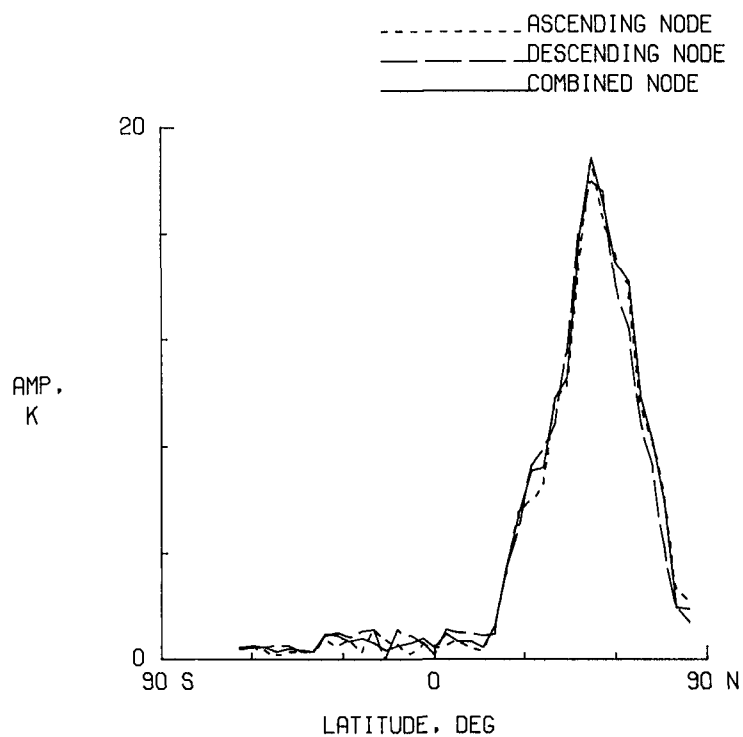


(a) Zonal mean amplitude.

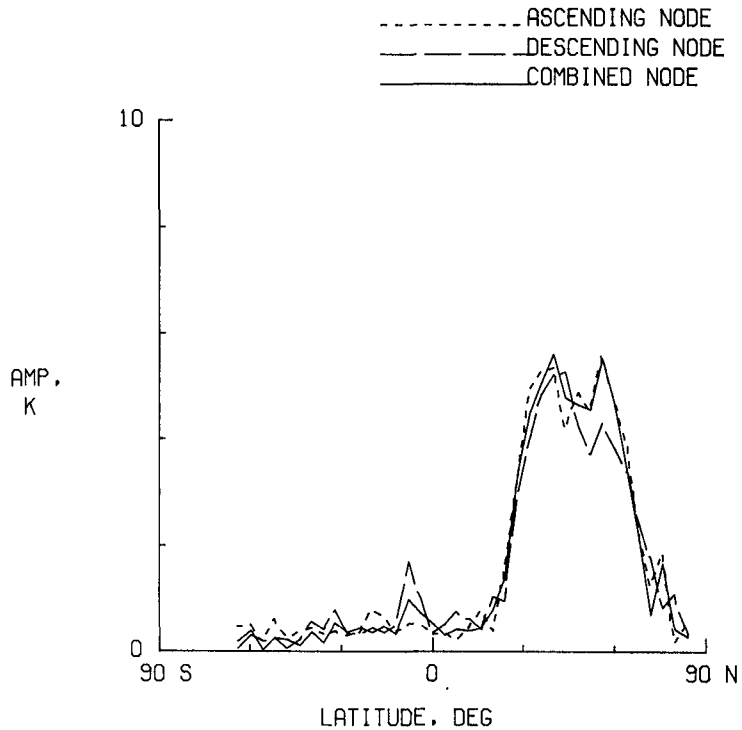


(b) Wave 1 amplitude.

Figure 14. Amplitude and phase of LAMAT temperatures for 3 mbar on Feb. 26, 1979.

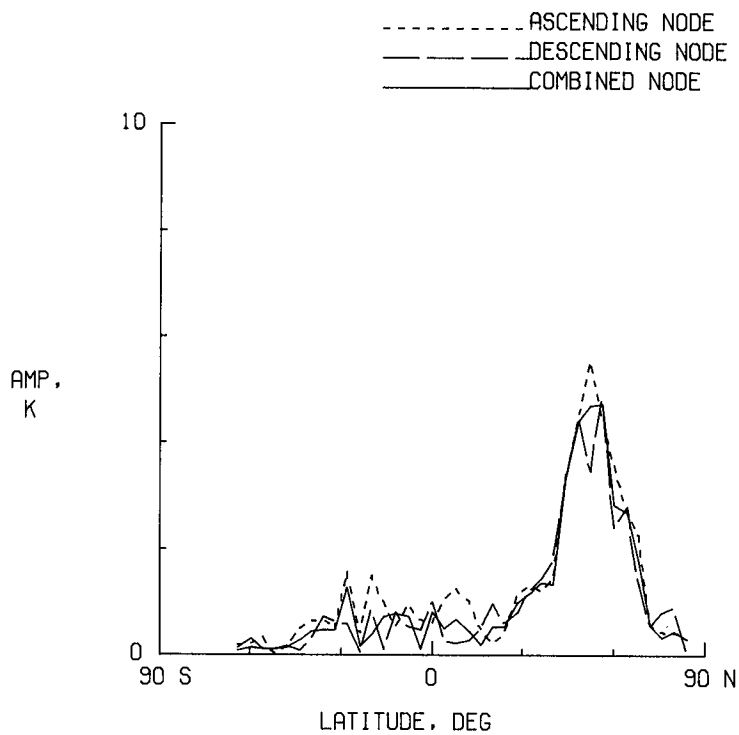


(c) Wave 2 amplitude.

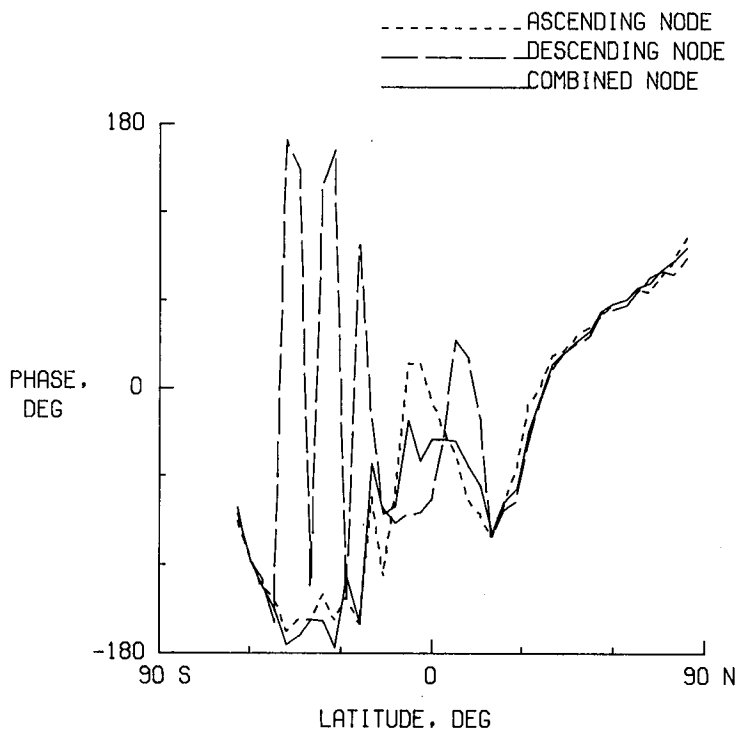


(d) Wave 3 amplitude.

Figure 14. Continued.

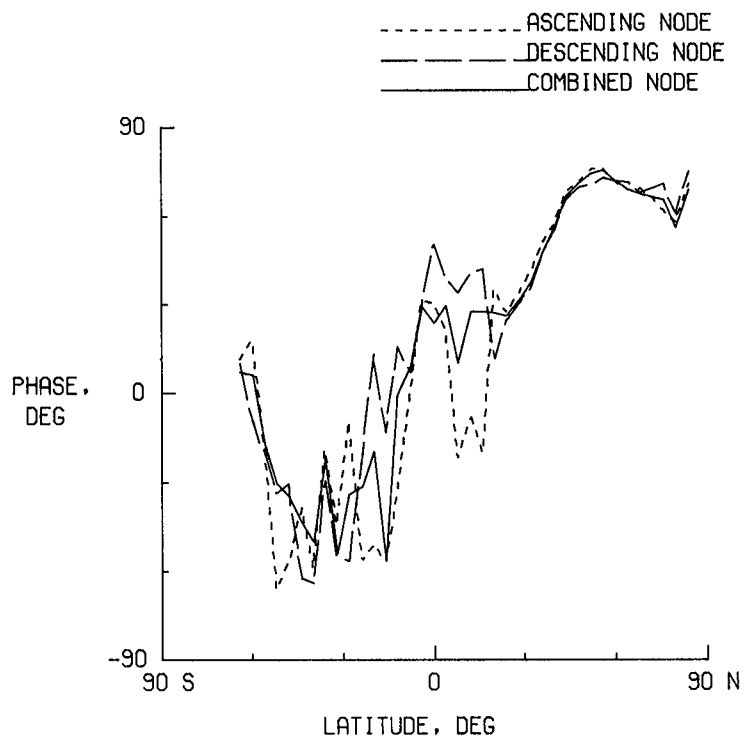


(e) Wave 4 amplitude.

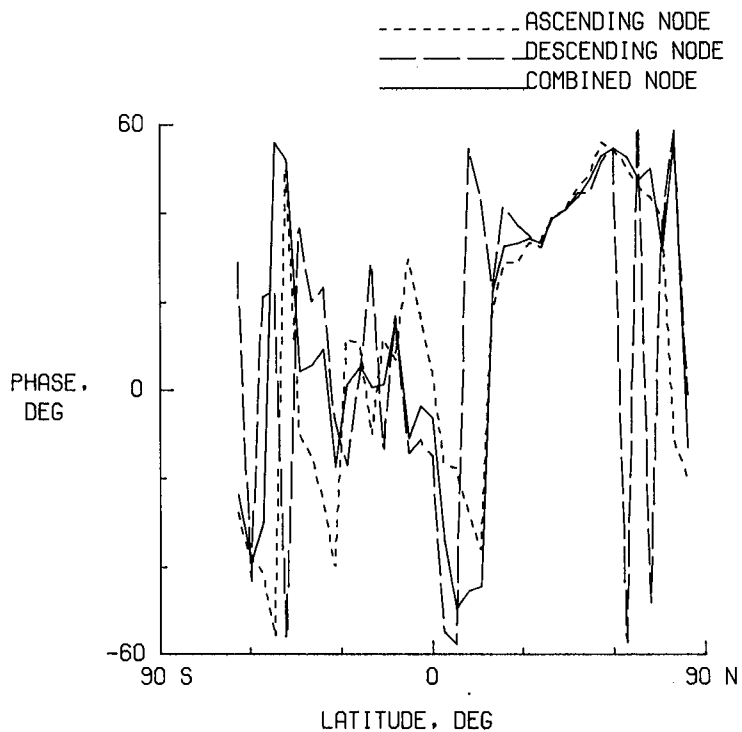


(f) Wave 1 phase.

Figure 14. Continued.

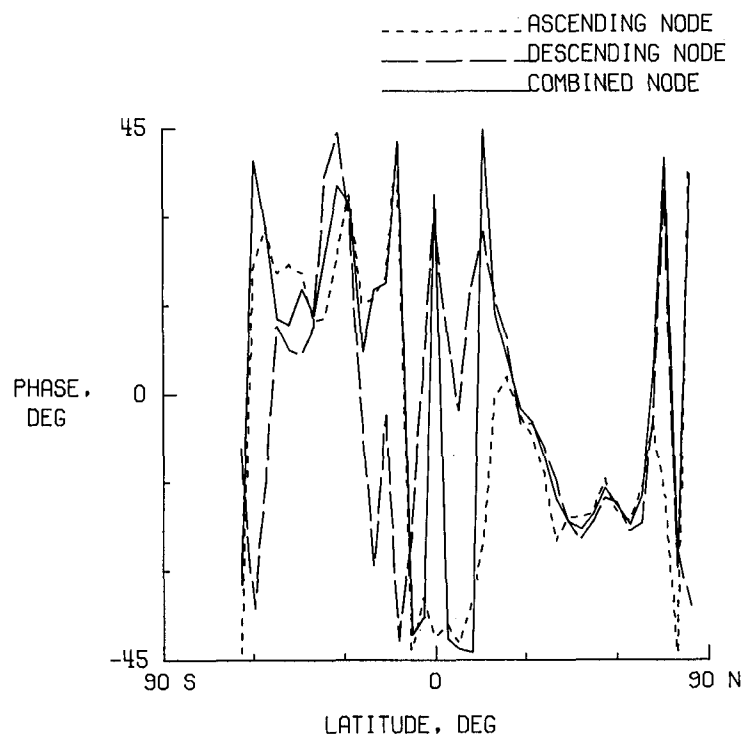


(g) Wave 2 phase.



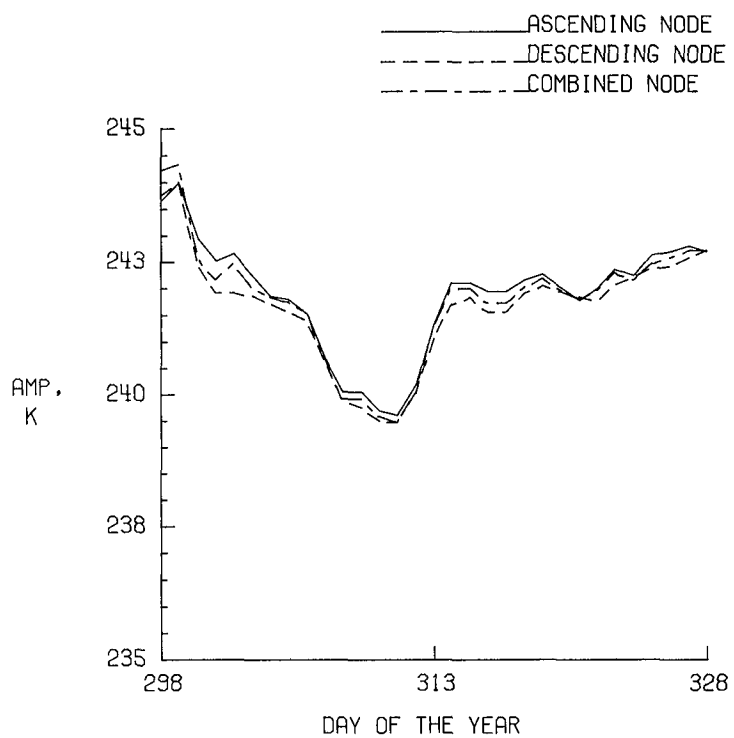
(h) Wave 3 phase.

Figure 14. Continued.

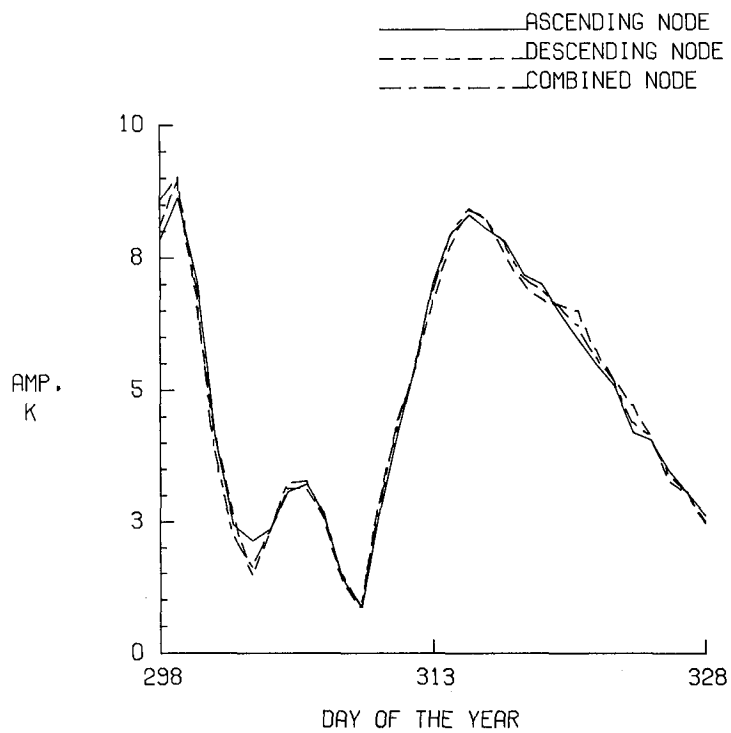


(i) Wave 4 phase.

Figure 14. Concluded.

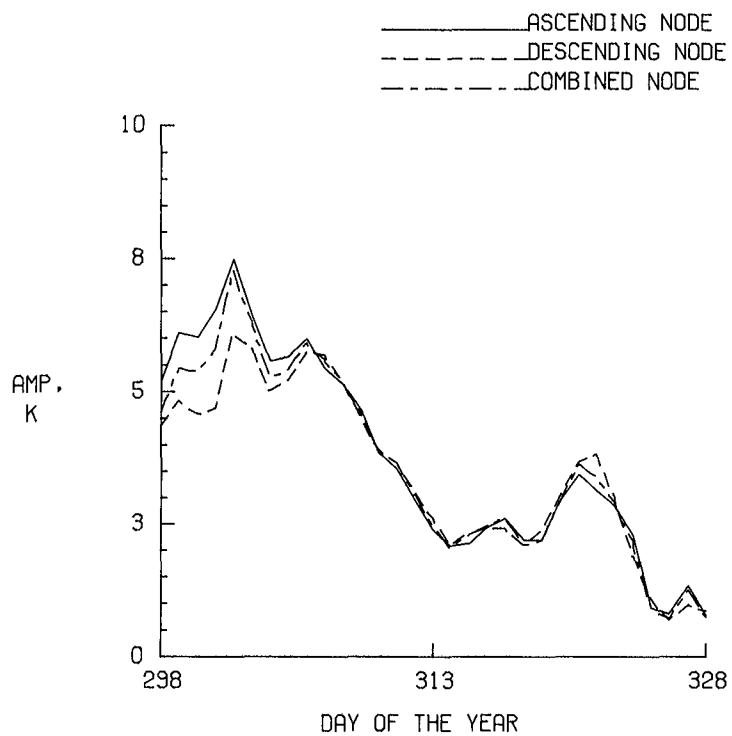


(a) Zonal mean amplitude.

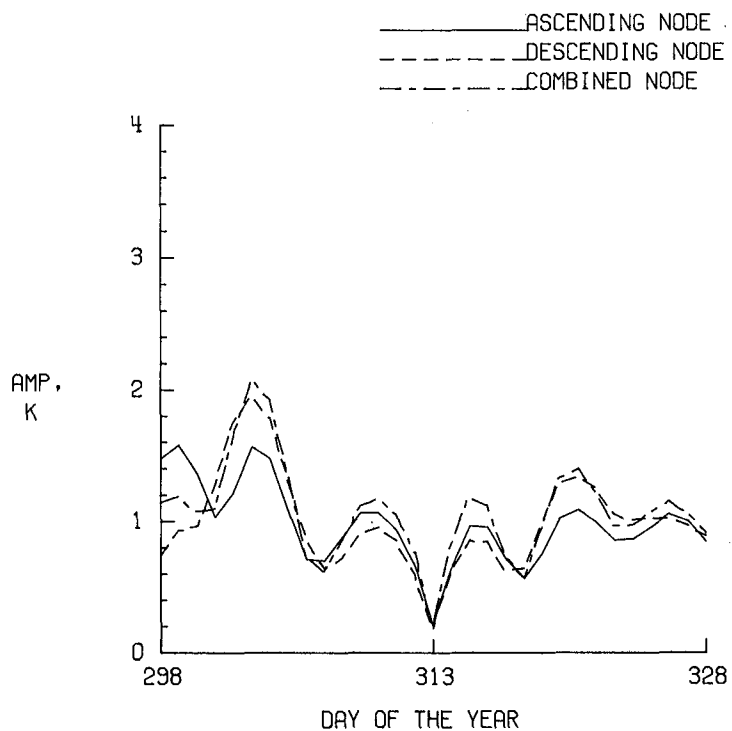


(b) Wave 1 amplitude.

Figure 15. Amplitude and phase of LAMAT temperature for 10 mbar, 64°S on Oct. 25 to Nov. 25, 1978.

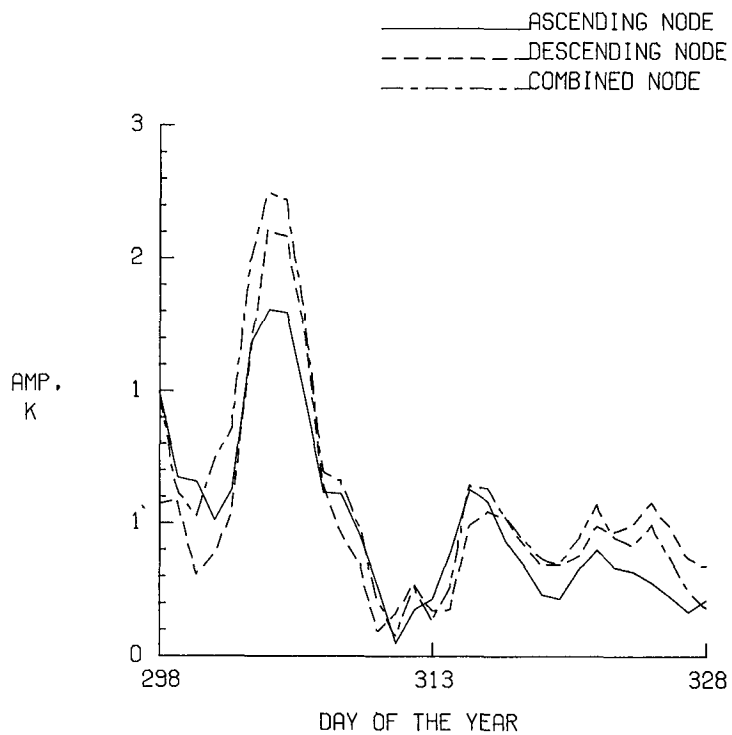


(c) Wave 2 amplitude.

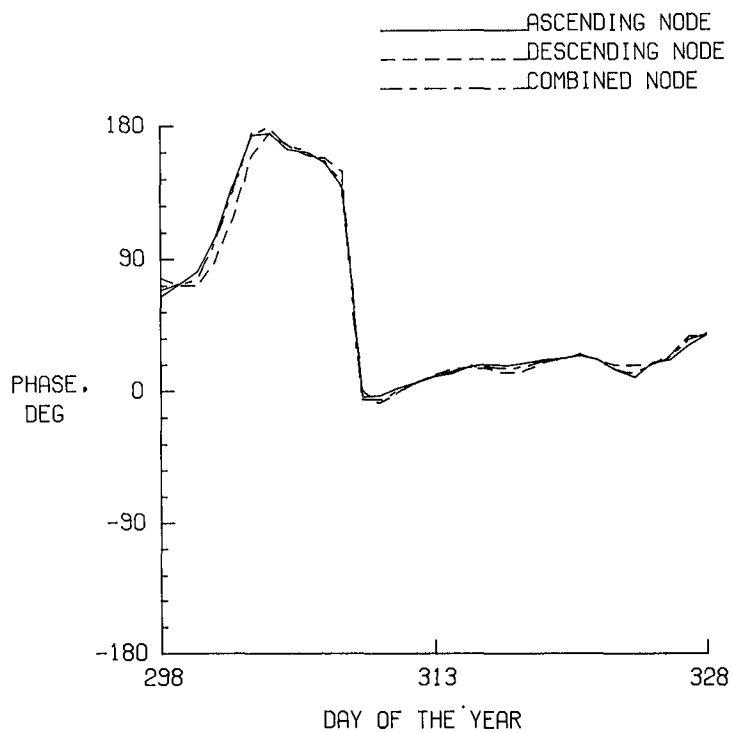


(d) Wave 3 amplitude.

Figure 15. Continued.

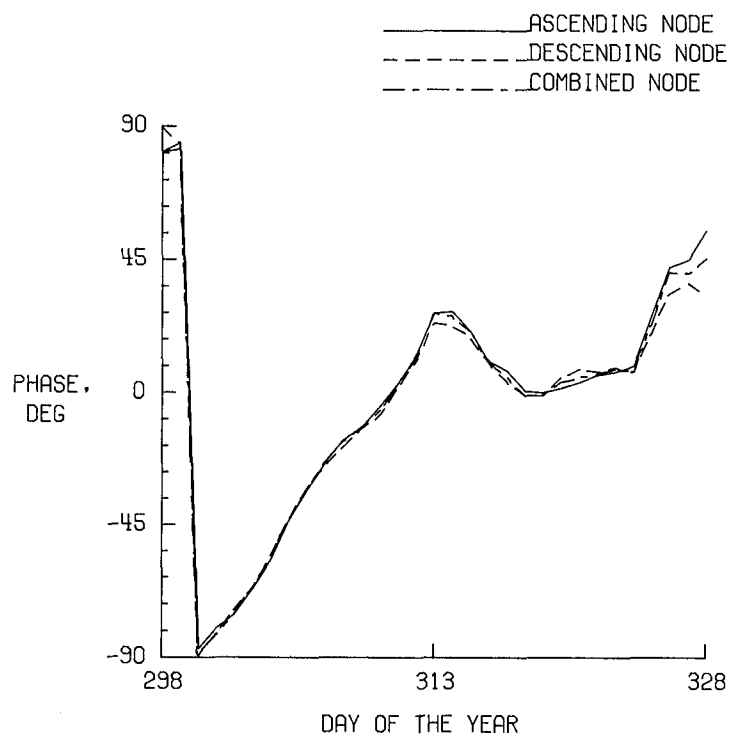


(e) Wave 4 amplitude.

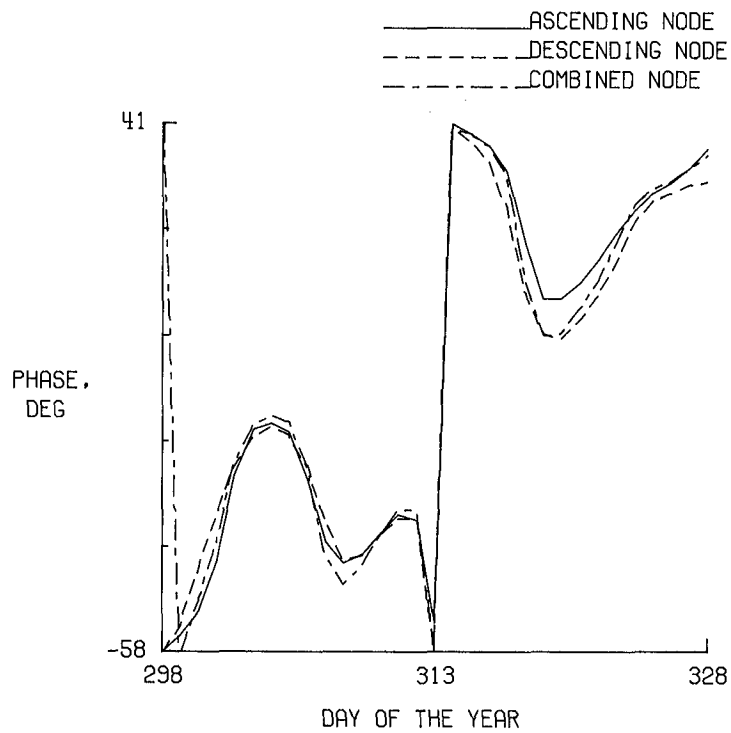


(f) Wave 1 phase.

Figure 15. Continued.

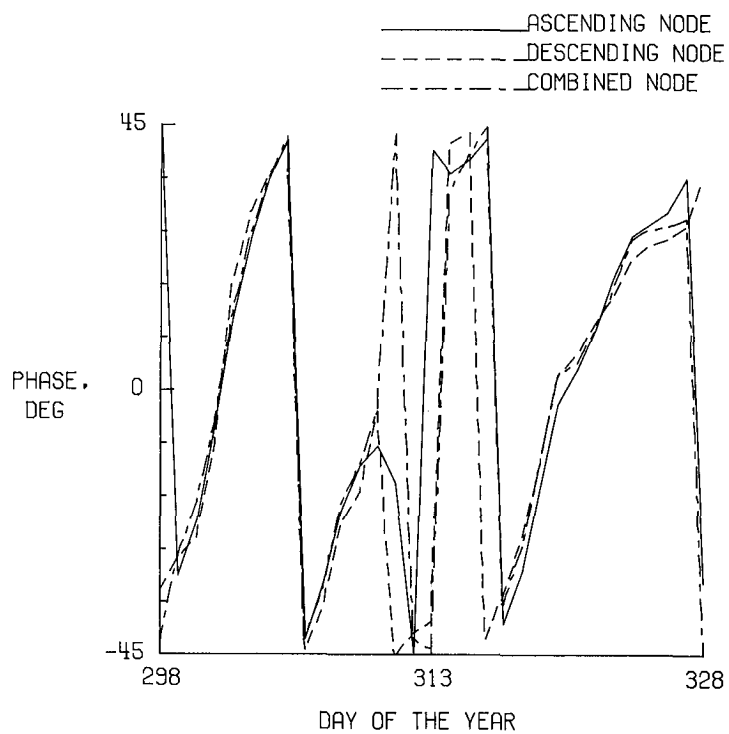


(g) Wave 2 phase.



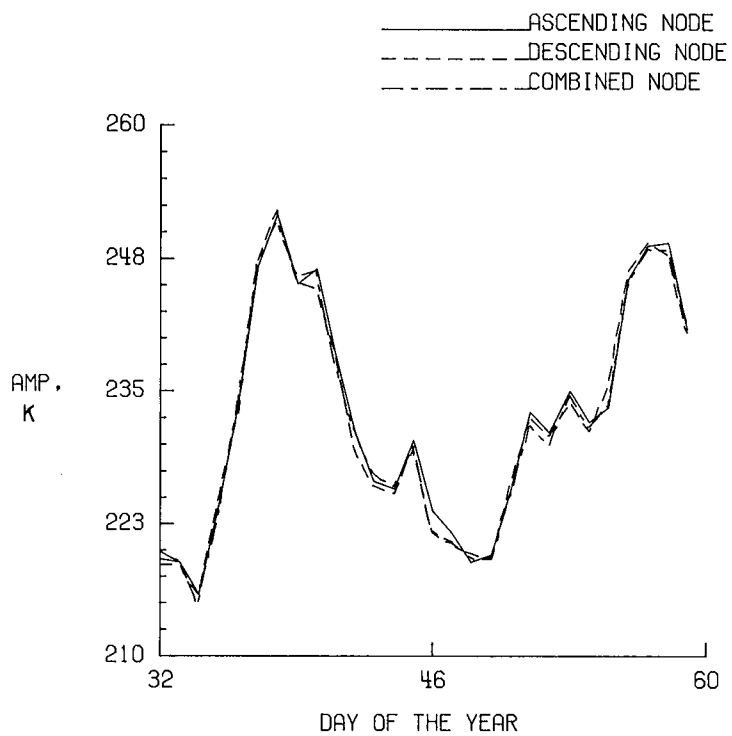
(h) Wave 3 phase.

Figure 15. Continued.

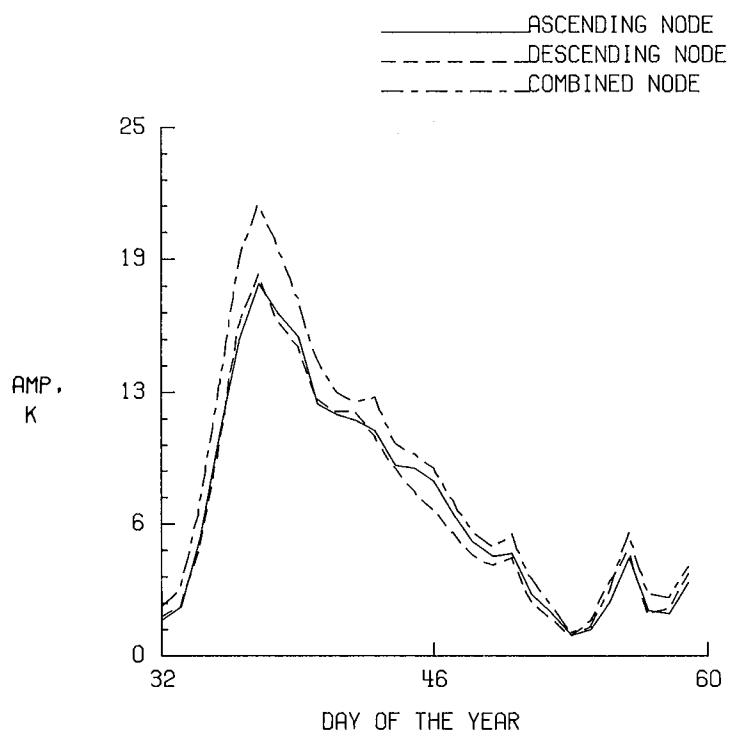


(i) Wave 4 phase.

Figure 15. Concluded.

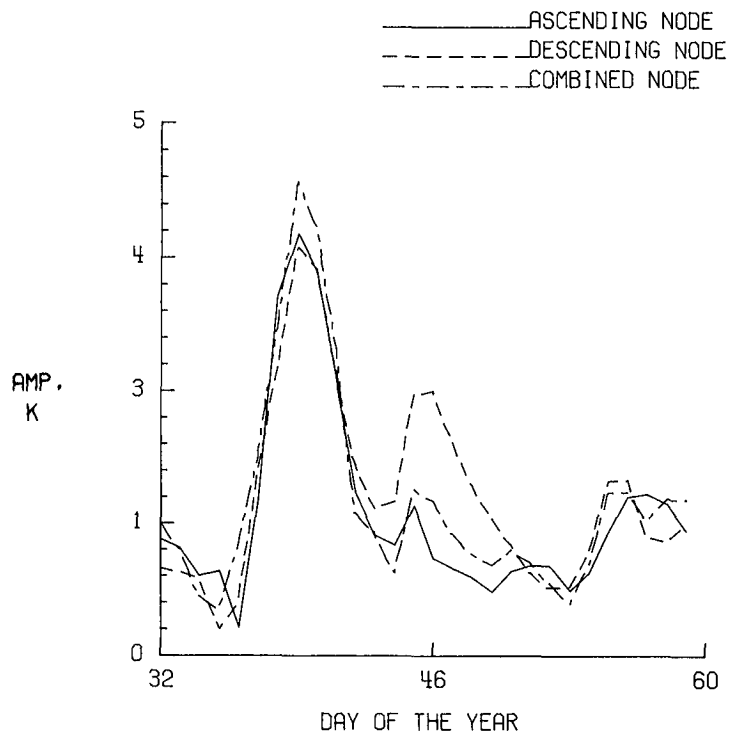


(a) Zonal mean.

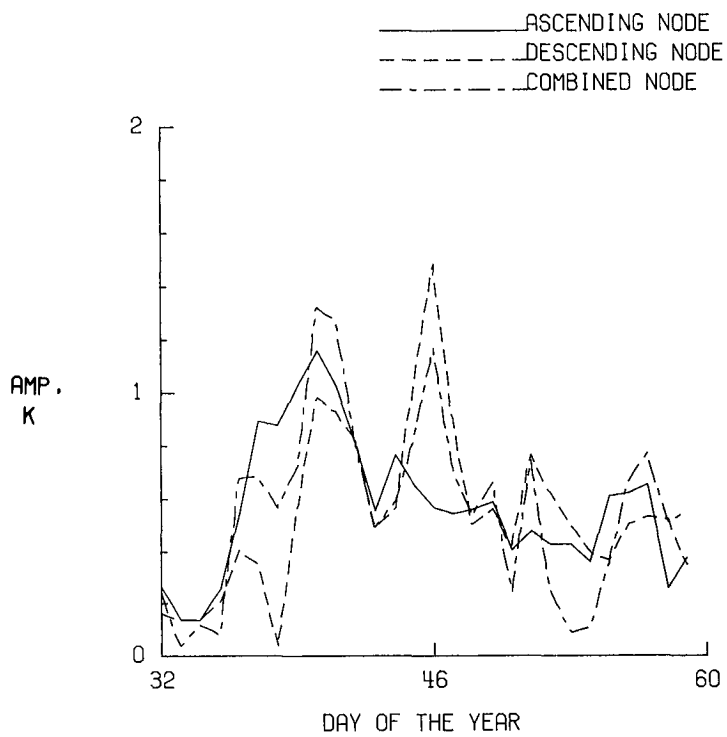


(b) Wave 1.

Figure 16. Amplitude of LAMAT temperature for 10 mbar, 83.5°N from Feb. 1 to Mar. 1, 1979.

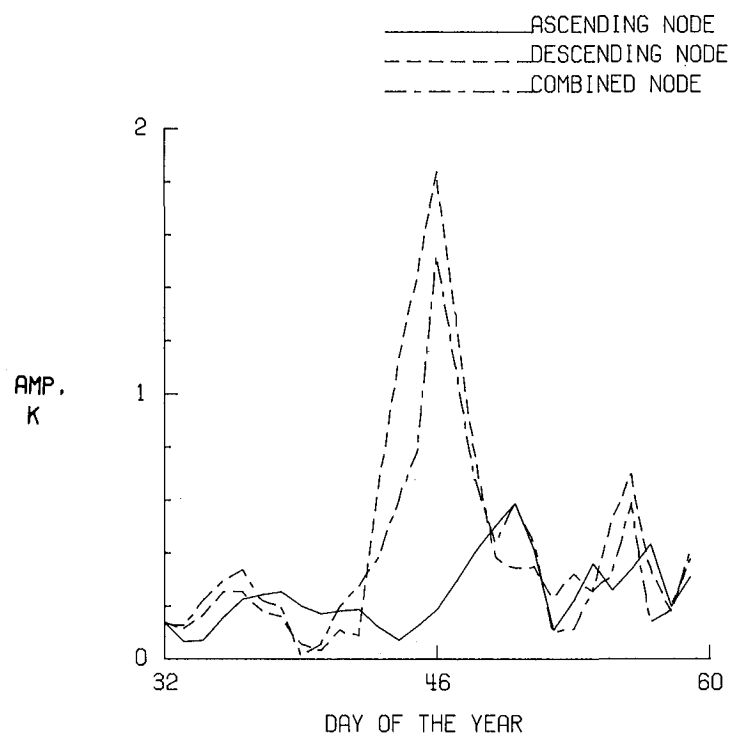


(c) Wave 2.



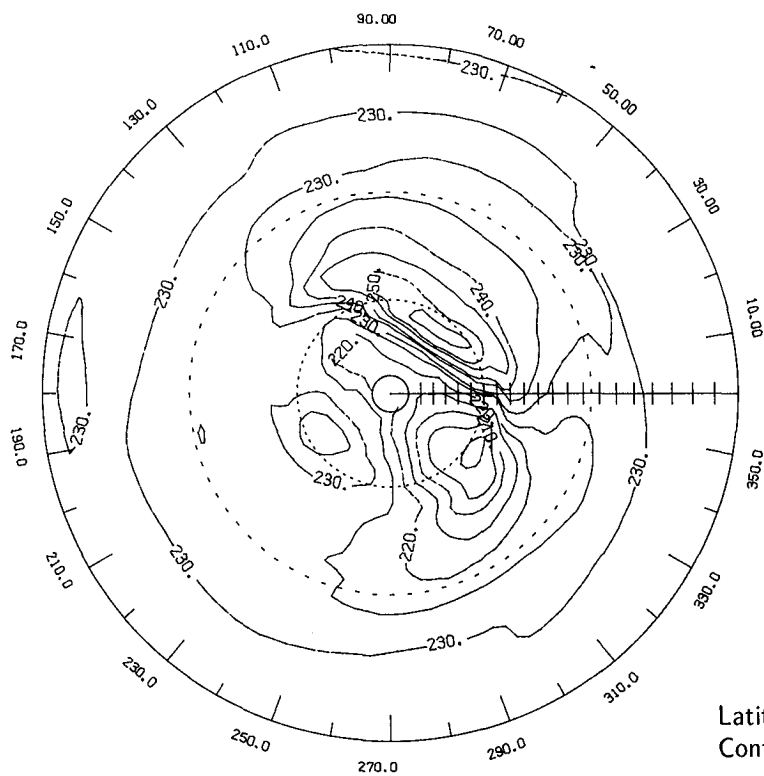
(d) Wave 3.

Figure 16. Continued.

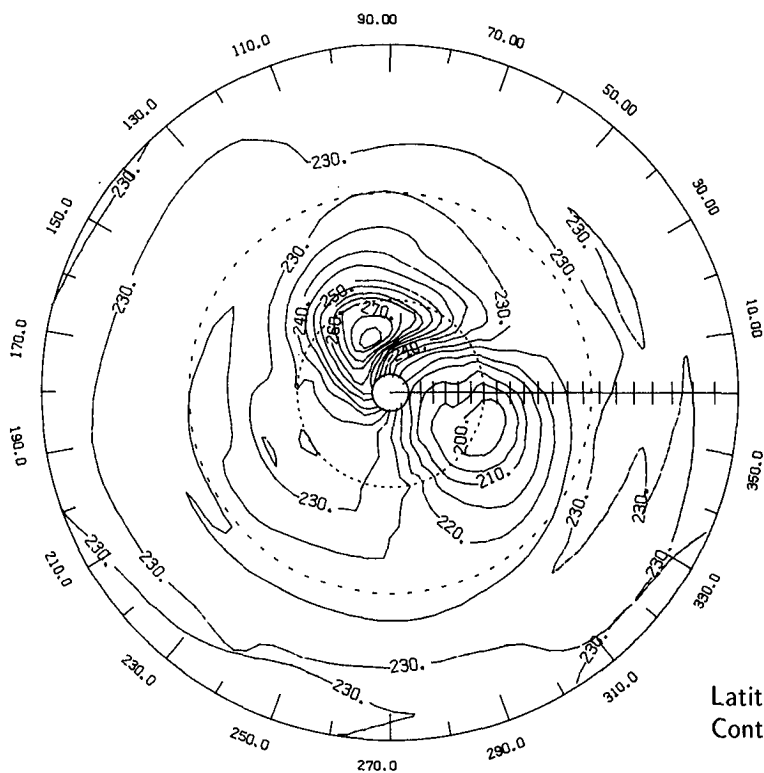


(e) Wave 4.

Figure 16. Concluded.

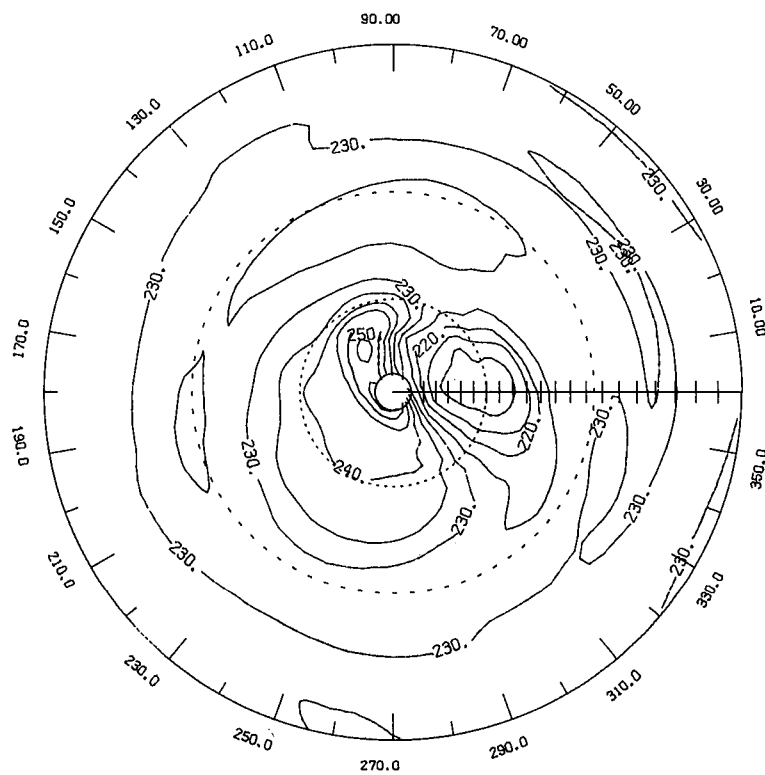


(a) Feb. 1, 1979.



(b) Feb. 5, 1979.

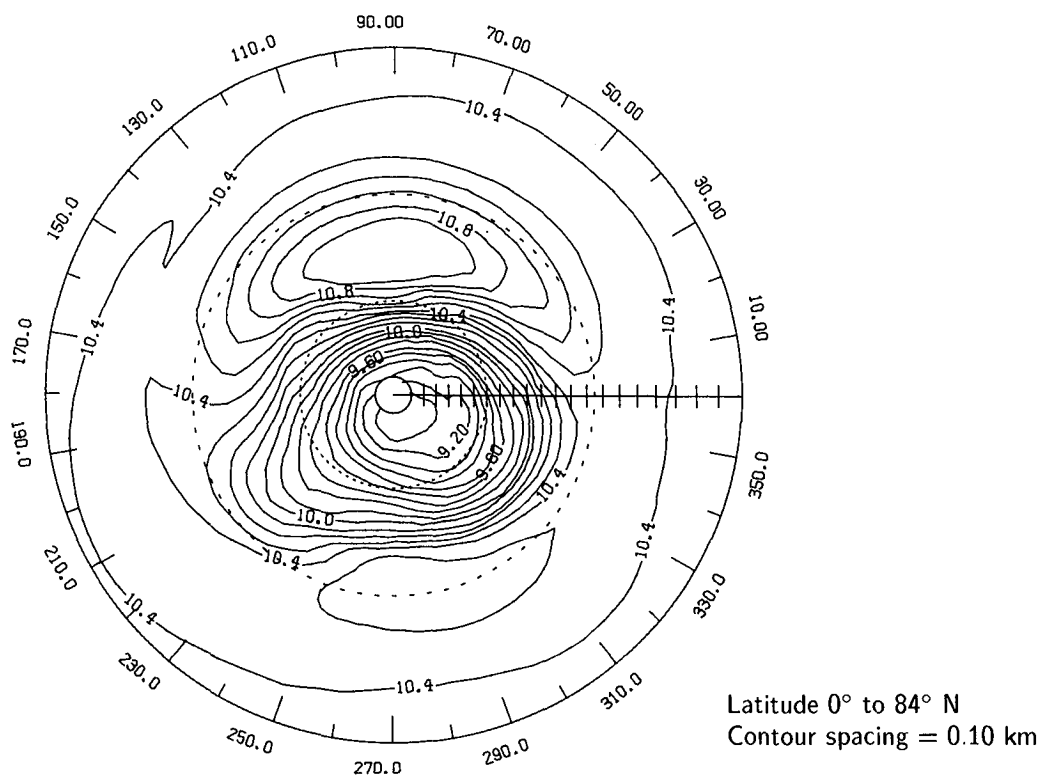
Figure 17. Stereographic maps of 10-mbar Northern Hemisphere LAMAT temperature from combined node.



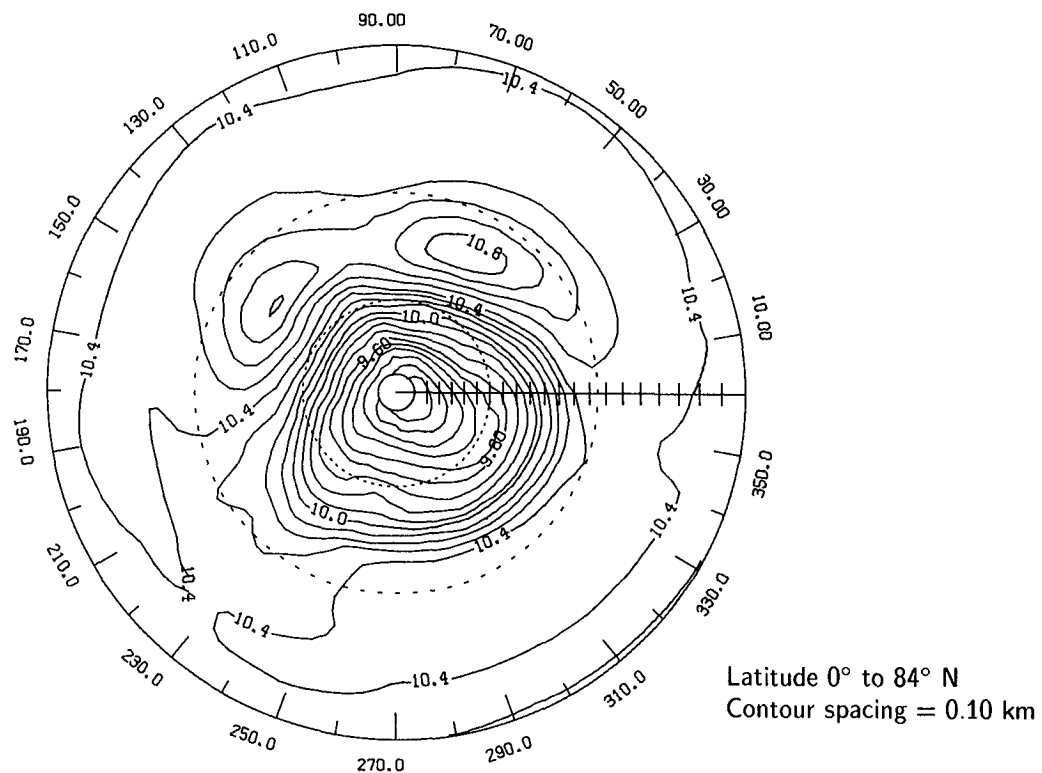
Latitude 0° to 84° N
Contour spacing = 5.00 K

(c) Feb. 9, 1979.

Figure 17. Concluded.

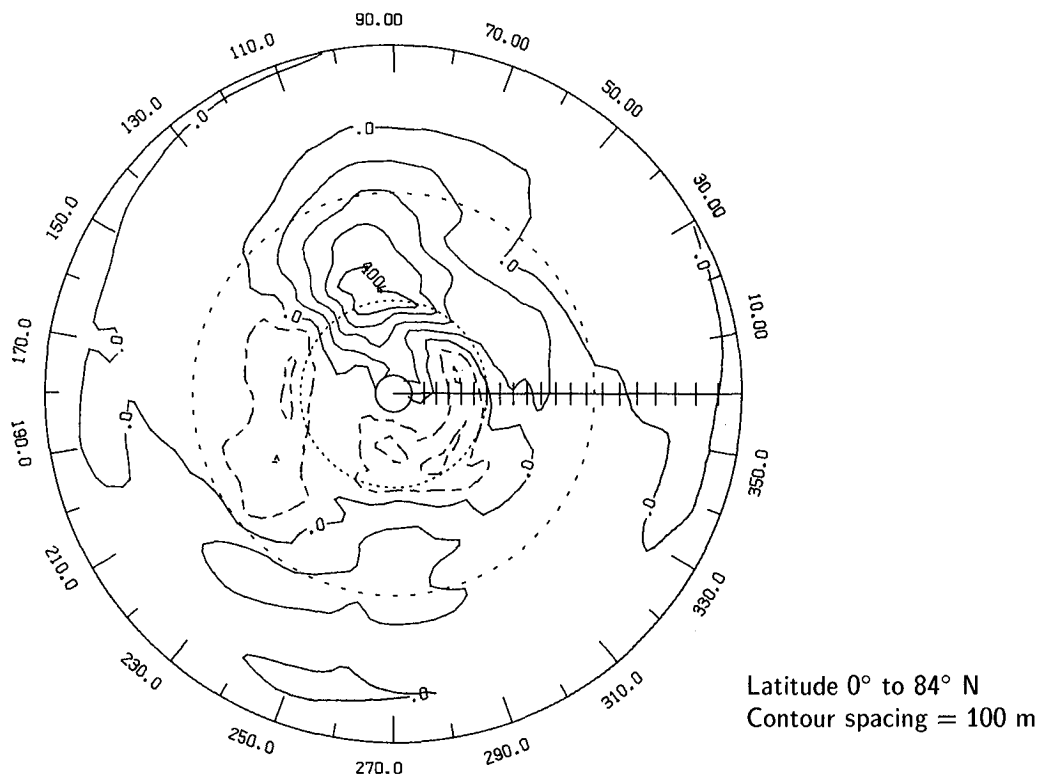


(a) LAMAT 50- to 10-mbar thickness on Jan. 2, 1979.

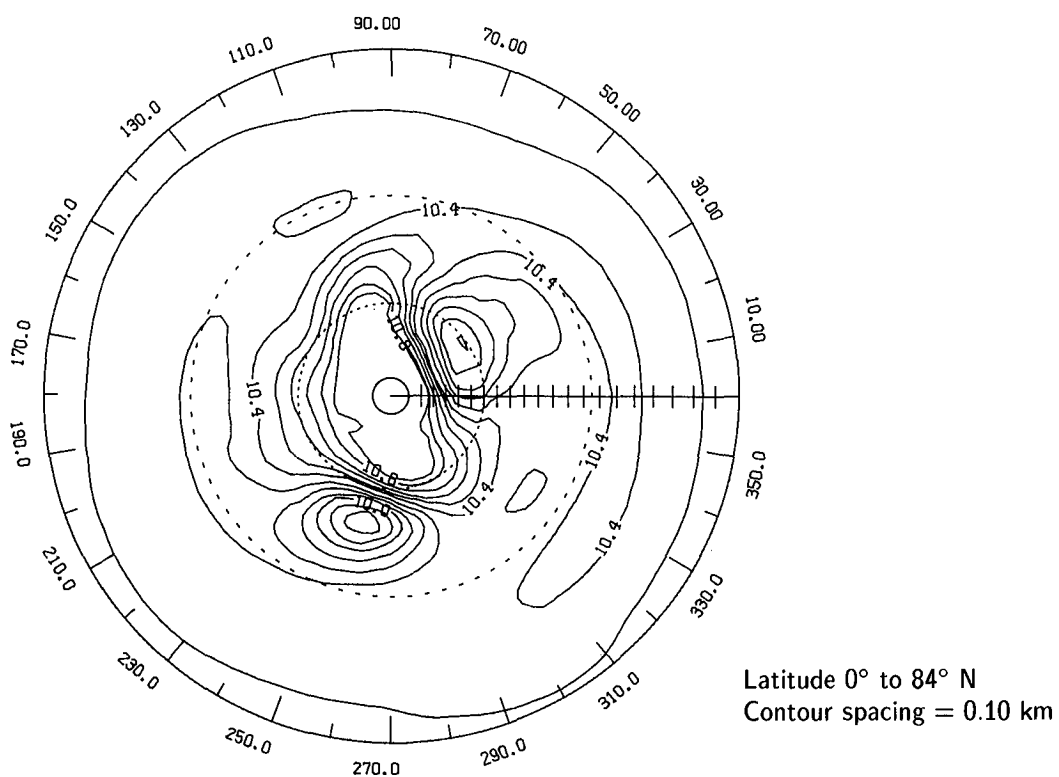


(b) Berlin 50- to 10-mbar thickness on Jan. 2, 1979.

Figure 18. Stereographic maps of Northern Hemisphere thickness fields.

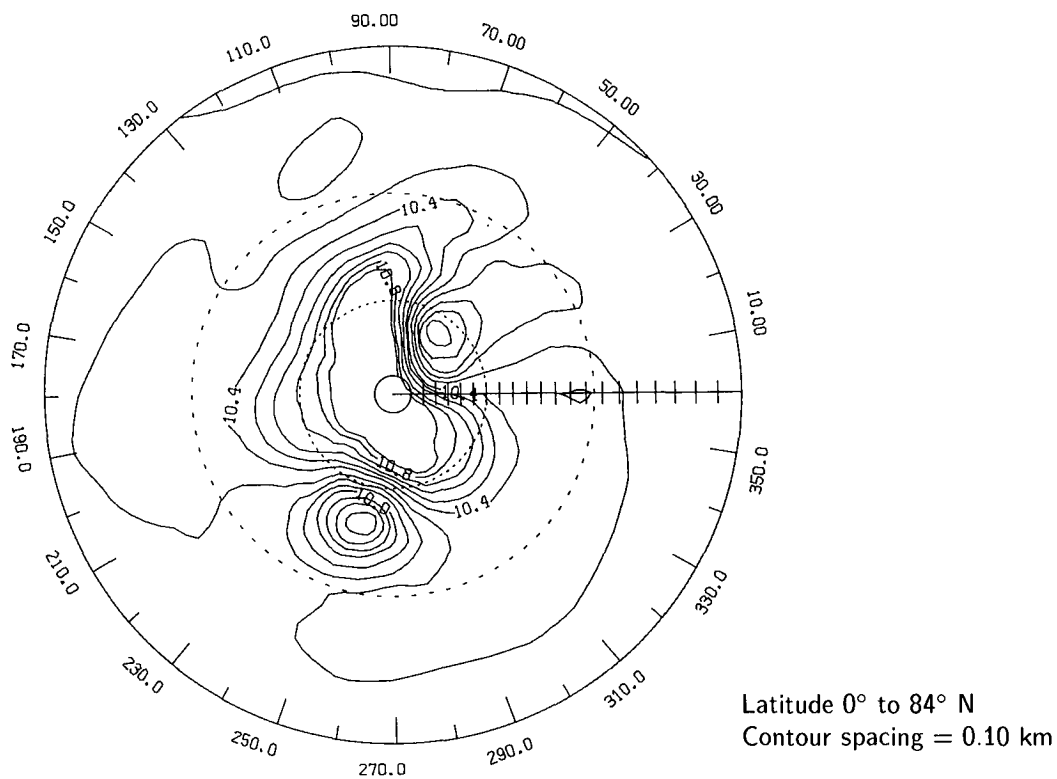


(c) Difference between LAMAT and Berlin thicknesses on Jan. 2, 1979.

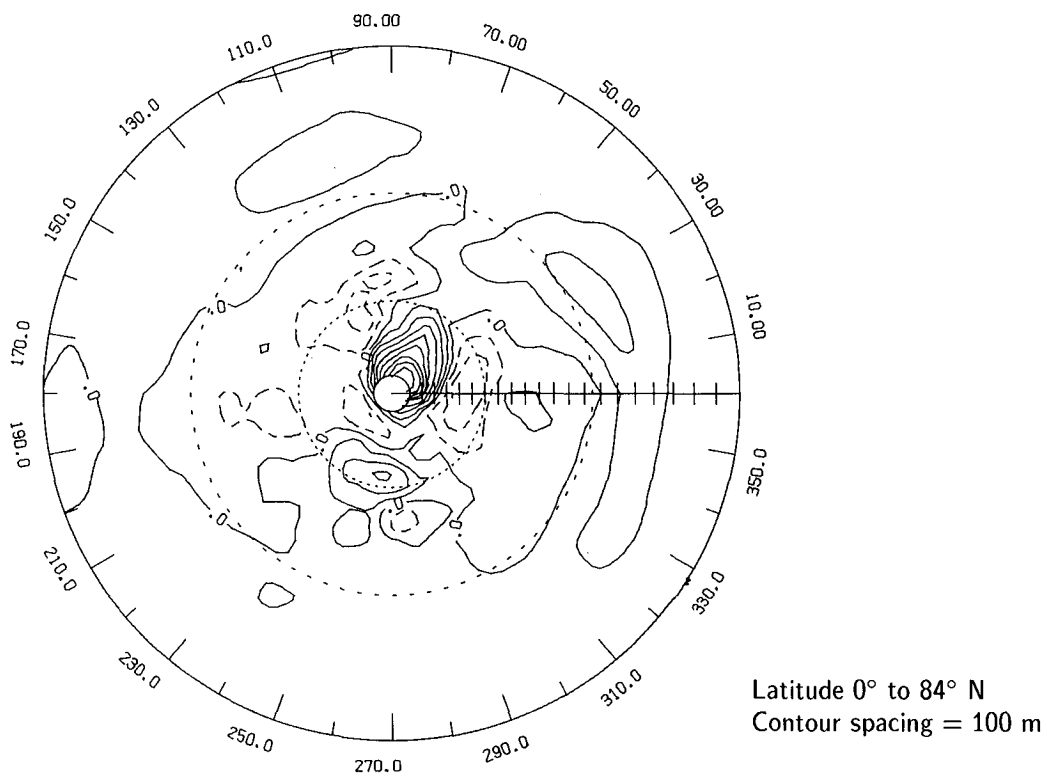


(d) LAMAT 50- to 10-mbar thickness on Feb. 26, 1979.

Figure 18. Continued.



(e) Berlin 50- to 10-mbar thickness on Feb. 26, 1979.



(f) Difference between LAMAT and Berlin thicknesses on Feb. 26, 1979.

Figure 18. Concluded.

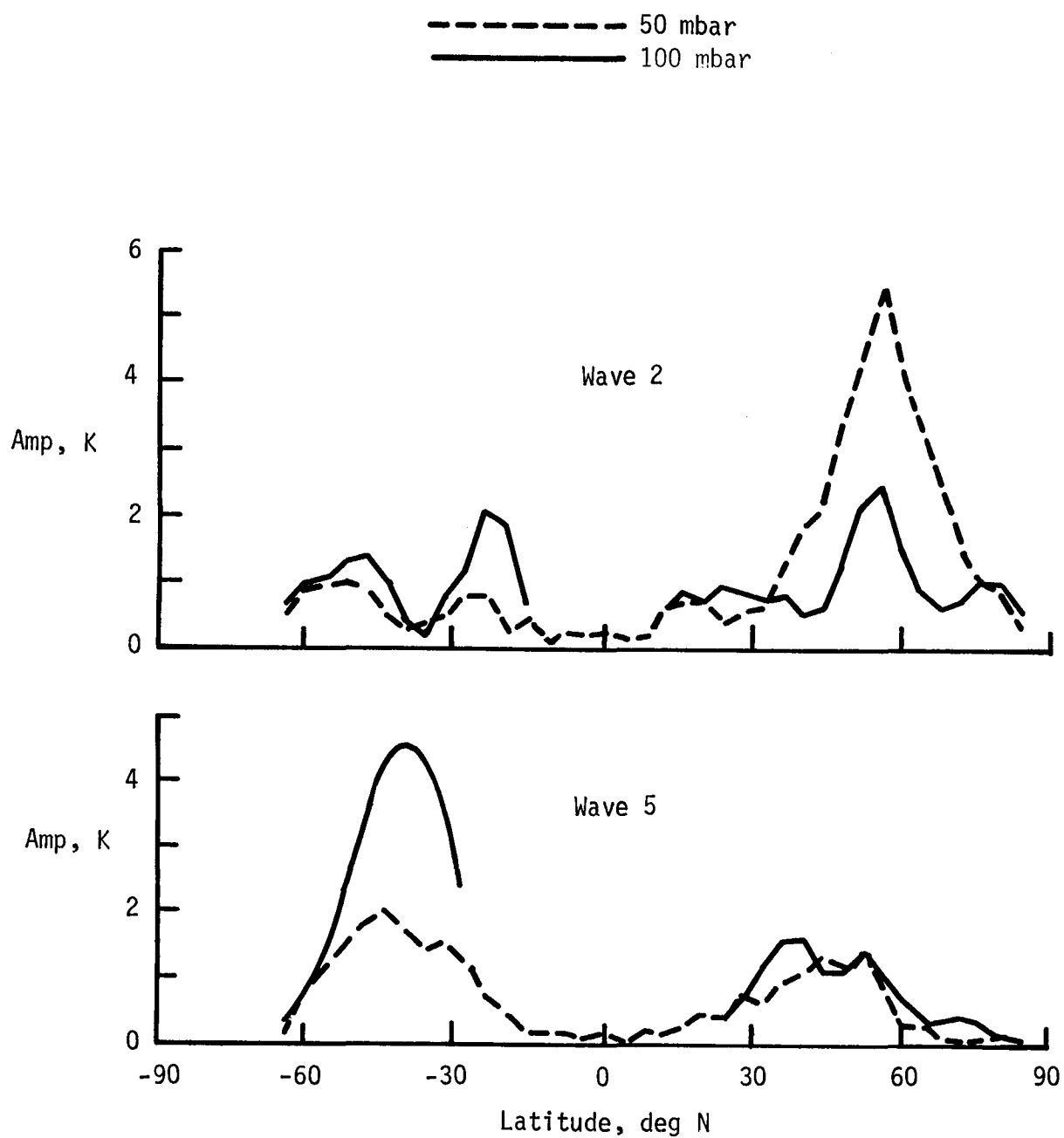


Figure 19. Wave 2 and 5 amplitudes of 100-mbar and 50-mbar LAMAT temperature on Jan. 7, 1979.

Standard Bibliographic Page

1. Report No. NASA TP-2553		2. Government Accession No.		3. Recipient's Catalog No.	
4. Title and Subtitle Description of Data on the Nimbus 7 LIMS Map Archive Tape— Temperature and Geopotential Height		5. Report Date May 1986		6. Performing Organization Code 673-41-10-70	
		8. Performing Organization Report No. L-16071			
7. Author(s) Kenneth V. Haggard, Ellis E. Remsburg, William L. Grose, James M. Russell III, B. T. Marshall, and G. Lingenfelter		10. Work Unit No.		11. Contract or Grant No.	
9. Performing Organization Name and Address NASA Langley Research Center Hampton, VA 23665-5225		13. Type of Report and Period Covered Technical Paper		14. Sponsoring Agency Code	
12. Sponsoring Agency Name and Address National Aeronautics and Space Administration Washington, DC 20546-0001		15. Supplementary Notes Kenneth V. Haggard, Ellis E. Remsburg, William L. Grose, and James M. Russell III: Langley Research Center, Hampton, Virginia. B. T. Marshall: SASC Technologies, Inc., Hampton, Virginia. G. Lingenfelter: Analytical Mechanics Assoc., Inc., Hampton, Virginia.			
16. Abstract This paper describes the process by which the analysis of the Limb Infrared Monitor of the Stratosphere (LIMS) experiment data were used to produce estimates of synoptic maps of temperature and geopotential height. In addition to a detailed description of the analysis procedure, this paper discusses several interesting features in the data and uses these features to demonstrate how the analysis procedure produced the final maps and how one can estimate the uncertainties in the maps. In addition, features in the analysis are noted that would influence how one might use, or interpret, the results. These include subjects such as smoothing and the interpretation of wave components. While some suggestions are made for an improved analysis of the data, it is shown that, in general, the maps are an excellent estimation of the synoptic fields.					
17. Key Words (Suggested by Authors(s)) LIMS (Limb Infrared Monitor of the Stratosphere) Nimbus 7 Kalman filter			18. Distribution Statement Unclassified—Unlimited		
19. Security Classif.(of this report) Unclassified			20. Security Classif.(of this page) Unclassified		21. No. of Pages 53
					22. Price A04
Subject Category 47					

**National Aeronautics and
Space Administration
Code NIT-4**

**Washington, D.C.
20546-0001**

**Official Business
Penalty for Private Use, \$300**

**BULK RATE
POSTAGE & FEES PAID
NASA
Permit No. G-27**



**POSTMASTER: If Undeliverable (Section 158
Postal Manual) Do Not Return**
